

PB-230 000

CORRELATION OF SIDE-FORCE AND YAWING-
MOMENT DATA FOR TACV CONFIGURATIONS
AT LARGE ANGLES OF SIDESLIP

J. Ray Ruetenik

Kaman AvIDyne

Prepared for:

Department of Transportation

January 1974

DISTRIBUTED BY:

NTIS

National Technical Information Service
U. S. DEPARTMENT OF COMMERCE
5285 Port Royal Road, Springfield Va. 22151

1. Report No. FRA-ORD&D-74-29		2. Government Accession No. PB 230 000	
4. Title and Subtitle CORRELATION OF SIDE-FORCE AND YAWING-MOMENT DATA FOR TACV CONFIGURATIONS AT LARGE ANGLES OF SIDESLIP		5. Report Date January 1974	
7. Author(s) *J. Ray Ruetenik		6. Performing Organization Code	
9. Performing Organization Name and Address Kaman Avidyne Division Kaman Sciences Corporation 83 Second Avenue Burlington MA 01803		8. Performing Organization Report No. DOT-TSC-UMTA-72-11	
12. Sponsoring Agency Name and Address Department of Transportation Urban Mass Transportation Administration Office of Research, Development & Demonstrations Washington DC 20590		10. Work Unit No. (TRIS) RR418/R4334	
15. Supplementary Notes *Under contract to: Department of Transportation Transportation Systems Center Kendall Square Cambridge MA 02142		11. Contract or Grant No. DOT-TSC-171	
16. Abstract Methods developed by Woolard and Ruetenik and Zartarian for predicting the side force and yawing moment on TACV configurations due to side winds are compared against available data from wind-tunnel tests. The predicted side force based on slender-body theory is found in good agreement with the data from moving-ground plane tests for sideslip angles less than 5 degrees. Above 5 degrees, fair agreement is found by incorporating viscous-cross flow effects in the theory, although characteristic differences are observed from previous correlations for missile-type bodies. The measured yawing moment is 15 to 35 percent less than the slender-body prediction, and it differs markedly from viscous-flow predictions. Data from tests with an elevated inverted-tee guideway correlate similarly. But test data from an elevated channel guideway differ considerably from the other correlations, indicating the need for systematic tests on the effect of side rails on the air loads for various vehicle configurations. Verification is needed of the present wind-tunnel testing techniques for the simulation of side-wind effects on high-speed ground vehicles on guideways. A study is made, therefore, of concepts for performing tests of full-scale air cushion vehicles for cross wind conditions.		13. Type of Report and Period Covered Final Report Sept 1971 - June 1972	
17. Key Words Tracked Air Cushion Vehicles Cross Winds Gust Loadings		14. Sponsoring Agency Code	
19. Security Classif. (of this report) Unclassified		18. Distribution Statement DOCUMENT IS AVAILABLE TO THE PUBLIC THROUGH THE NATIONAL TECHNICAL INFORMATION SERVICE, SPRINGFIELD VIRGINIA 22151	
20. Security Classif. (of this page) Unclassified		21. No. of Pages 70	
		22. Price \$3.75-1.45	

NOTICE

This document is disseminated under the sponsorship of the Department of Transportation in the interest of information exchange. The United States Government assumes no liability for its contents or use thereof.

PREFACE

This research was carried out by the Kaman Avidyne Division of Kaman Sciences Corporation, Burlington, Massachusetts, for the Department of Transportation, Transportation Systems Center, Cambridge, Massachusetts, under Contract No. DOT-TSC-171. Dr. Timothy M. Barrows of the Technology Directorate, Power and Propulsion Branch, served as the technical monitor.

Dr. J. Ray Ruetenik was the Project Leader under Dr. Norman P. Hobbs, Technical Director of Kaman Avidyne. The author would like to express appreciation for the constructive guidance provided by Dr. Barrows through the technical reviews during the progress of this work.

TABLE OF CONTENTS

<u>SECTION</u>		<u>PAGE</u>
1	INTRODUCTION	1
2	THEORETICAL METHODS FOR PREDICTING SIDE-WIND FORCES	3
	2.1 Woolard Equation (Reference 9)	3
	2.2 Equations of Ruetenik and Zartarian (Reference 1)	4
3	CORRELATION OF EXPERIMENTAL DATA	7
	3.1 Grunwald Data of NASA TN D-5935 (Reference 3)	7
	3.2 Grunwald Data of NASA TN D-6011 (Reference 6)	13
	3.3 Tracked Hovercraft Limited Data of FRA-RT-71-68 (Reference 7)	14
	3.4 Grumman TACRV Data (Reference 8)	17
4	CONCLUSIONS	19
5	APPENDIX	21
6	REFERENCES	25
7	FIGURES	27

LIST OF ILLUSTRATIONS

<u>Figure</u>		<u>Page</u>
1.	Sketch of Representative Vehicle Constructed for Basis of Analysis.....	27
2.	Drawing of Axis System Showing Positive Direction of Forces, Moments, and Angles NASA TN D-5935.....	28
3.	Configuration of Six Models Employed in Tests by Grunwald, NASA TN D-5935.....	29
4.	Aerodynamic Coefficient Based on Maximum Cross-Sectional Area as a Function of Gap Height Above Ground Plane for Six Configu- rations Tested by Grunwald, NASA TN D-5935..	35
5.	Aerodynamic Coefficient Based on Area of Circle Having Diameter Equivalent to Vehicle Height Plotted as Function of Gap Height Above Ground for Six Configurations Tested by Grunwald, NASA TN D-5935.....	37
6.	Variation of Aerodynamic Coefficient With Sideslip Angle for Half Circle-Cross Section Configuration.....	39
7.	Variation of Aerodynamic Coefficient With Sideslip Angle for Square Type-Cross Section Configuration.....	41
8.	Variation of Aerodynamic Coefficient With Sideslip Angle for Circular-Cross Section Configuration.....	43
9.	Effect of Splitter Plate in Wake of Cir- cular Cylinder on Pressure.....	45
10.	Sketches of Three Models Employed by Grunwald and Johnson, NASA TN D-6011.....	47
11.	Variation of Aerodynamic Coefficient With Sideslip Angle for Rectangular Air-Cushion Models.....	50

LIST OF ILLUSTRATIONS (Concluded)

<u>Figure</u>		<u>Page</u>
12.	Variation of Aerodynamic Coefficients With Sideslip Angle for Side-by-Side Air Cushion Models.....	52
13.	Dimensions of Track and Vehicle Models, THL, FRA-RT-71-68.....	54
14.	Dimensions of Track and Vehicle Models, THL, FRA-RT-71-68.....	55
15.	Effect of Yaw Angle on Sideforce and Yawing Moment Coefficients, Inverted T Configuration.....	56
16.	Effect of Yaw Angle on Sideforce and Yawing Moment Coefficients, Channel Configuration.....	57
17.	Sketch of 1/10-scale Model Used in Grumman Tests, PMT-B4-R71-06.....	58
18.	Variation of Aerodynamic Coefficients With Sideslip for TACRV Model.....	60
19.	Sketch of a Test Arrangement for Measur- ing Airloads due to Side Wind and Gust.....	62

SYMBOLS

- A_m maximum cross-sectional area
 A_r reference cross-sectional area, $\pi H_v^2/4$
 A_λ cross-sectional area at aft end
 C_n yawing-moment coefficient, $M_z/A_r Lq$
 \bar{C}_n based on maximum cross-sectional area, $M_z/A_m Lq$
 C_Y side-force coefficient, $Y/A_r q$
 \bar{C}_Y based on maximum cross-sectional area, $Y/A_m q$
 H nominal height setting of model from ground belt
 (NASA TN D-5935)
 L body length
 M_z yawing moment (Fig. 1)
 V vehicle velocity
 Y side force
 d_e diameter of a circle with cross-sectional area equivalent
 to maximum cross-sectional area of model (NASA TN D-5935)
 g function in Equations (4) and (5)
 $\left. \begin{matrix} h_v \\ H_v \\ \bar{h}_v \end{matrix} \right\}$ vehicle or body local, maximum and reduced height, $\bar{h}_v = h_v/H_v$
 h_w side-rail height
 k constant in Equations (4) and (5)

- q dynamic pressure, $\rho v_r^2/2$
 r_w side-rail factor
 v_c side-wind velocity
 v_r relative velocity, $\sqrt{v^2 + v_c^2}$
 w_v vehicle local width
 x, z longitudinal and vertical coordinates (Figure 1)
 β sideslip angle
 γ nondimensional wall height, h_w/H_v
 λ reduced body length, L/H_v
 λ_1 reduced length of body nose (Figure 1)
 ξ, ζ reduced coordinates; $\xi = x/H_v$, $\zeta = z/H_v$
 ξ_1 ξ -coordinate where side-rail equals body height

Subscripts

- c viscous, cross-flow value
 s slender-body value
 λ aft end of body

1. INTRODUCTION

High-speed ground vehicles, such as the tracked air cushion vehicles (TACV) under development by the U.S. Department of Transportation, may be design constrained by the forces due to side winds. Traveling at speeds of 150 to 300 miles per hour, side forces due to winds may require lateral constraint on the vehicle that could be a significant factor to air cushion costs, guideway costs, and cushion power requirements.

Ruetenik and Zartarian¹ developed a theoretical method for predicting the transient air forces on high-speed ground vehicles of TACV type due to side-wind gusts. The method is an extension of a theoretical method developed by Ruetenik and Brooks² for predicting the transient air forces on missile-type bodies due to indicial sinking (sudden angle of attack). The method of Ruetenik and Brooks also predicts the forces and moments due to a steady side wind, and comparisons made in reference 2 with experimental data showed good agreement for bodies to angles of attack as high as 25 degrees.

Data are not available on the air forces produced by side-wind gusts acting upon high-speed ground vehicles, so comparisons were made by Ruetenik and Zartarian¹ with the steady-state force data for TACV-type models from experiments performed by Grunwald³ where models were yawed in a wind tunnel using the Langley moving-belt facility. The steady-state side force predicted by Ruetenik and Zartarian¹ for a single body was 2.13 times the value measured by Grunwald³, whereas good correlation was found by reference 1 with the measurements made by Perkins and Jorgensen⁴ and Schindel⁵ on similar bodies in wind tunnels. The large overprediction of the side forces for these ground-vehicle models was attributed by reference 1 to ground-plane effects. It was concluded that the effect of a ground plane and other environmental features,

such as side rails, air cushions, ground-plane gap and vehicle configuration should be studied.

Other wind-tunnel data have become available from force and moment measurements on high-speed, ground-vehicle models. Measurements are reported by Grunwald⁶ for examining the effect of various air cushion types on the side-wind air forces. The Tracked Hovercraft Limited⁷ performed measurements on wind-tunnel models in an elevated track simulation with an inverted-tee section track and a channel-section track. Data have also been obtained by Grumman⁸ on a model of the tracked air cushion research vehicle (TACRV) being developed for the Federal Railroad Administration. The simulated TACRV vehicle uses a channel guideway and the vehicle has a body separate from the chassis with a simulated jet air-supply system mounted aft above.

One objective of the present study is to correlate all the available data with theoretical methods for predicting the steady-state side-force and yawing moment due to side winds. Two theoretical methods are available for correlation of high-speed ground vehicle data. Both methods include the effect of side rails. Woolard⁹ has developed a method for predicting the side force based on slender-body theory for a non-viscous fluid. Ruetenik and Zartarian¹ developed equations for predicting the side force and yawing moment using slender-body theory and accounting for the nonlinear viscous cross-flow effects from the wake on the lee side. These methods will be correlated with the data available for TACV-type configurations.

A second objective of this study is to investigate concepts for measuring the forces due to side winds on full-scale air cushion vehicles. This work is reported in the Appendix.

2. THEORETICAL METHODS FOR PREDICTING SIDE-WIND FORCES

A sketch of the features of a high-speed ground vehicle as reflected in the aerodynamic methods is shown in Figure 1. The local height of the vehicle is h_v and the maximum height is H_v . The gap between the vehicle and the ground plane is H , and the height of the side wall above the ground plane is h_w .

2.1 WOOLARD EQUATION (REFERENCE 9)

The equation for the steady-state side force, Y , given by Woolard⁹ for a side-wall height, h_w , and a vehicle height at the aft end, $h_{v\lambda}$, is

$$\begin{aligned} \frac{\pi}{\beta} \frac{Y}{qA_\lambda} = & -2\tau\pi \left[1 + \frac{1+\tau}{\tau^2} \gamma_\lambda^2 \right] + \\ & 4 \frac{1+\tau}{\tau} \left[\tau\gamma_\lambda (1 - \gamma_\lambda^2)^{1/2} + \gamma_\lambda^2 \tan^{-1} \left(\frac{\eta}{\tau} \right) \right] + \\ & \frac{4\tau}{1-\tau} \left[\tan^{-1} \left(\frac{\eta}{\tau} \right) - \tau \tan \eta \right] \\ & \text{for } \gamma_\lambda < 1 \\ & = 0 \quad \text{for } \gamma_\lambda \geq 1 \end{aligned} \tag{1}$$

where $\eta = \gamma_\lambda / (1 - \gamma_\lambda^2)^{1/2}$

$$\tau = 2h_v/w_v$$

$$\gamma = h_w/H_v, \quad \gamma_\lambda = h_w/h_{v\lambda}$$

and w_v is the local width of the vehicle, q is the dynamic pressure, β is the local side-slip angle, and $h_{v\lambda}$ and A_λ are the vehicle height and cross-sectional area, respectively, at the aft end.

Woolard specified that application of Equation (1) is limited to vehicles having similar semielliptic cross sections.⁹

In view of the need for a more general application, Equation (1) will be applied for predictions with differing cross sections as well by determining τ at the aft end of the body, that is taking $\tau = \tau_\lambda$ where $\tau_\lambda = 2 \times (h_V/w_V)_\lambda$.

2.2 EQUATIONS OF RUETENIK AND ZARTARIAN (REFERENCE 1)

Slender-Body Equations

The equations for the coefficients of the steady-state side force and yawing moment, M_z , given by Reference 1, derived assuming slender-body flow, are*

$$C_Y = 8 I_1(\gamma) \beta \quad (2)$$

$$C_n = 8 \left[I_1(\gamma) - \frac{I_3(\gamma)}{\lambda} \right] \beta \quad (3)$$

where

$$I_1(\gamma) = \int_{\xi_1}^{\lambda_1} \bar{h}_V(\xi) \bar{h}'_V(\xi) r_{ws}(\xi, \gamma) d\xi$$

$$I_3(\gamma) = \int_{\xi_1}^{\lambda_1} \xi \bar{h}_V(\xi) \bar{h}'_V(\xi) r_{ws}(\xi, \gamma) d\xi$$

$$r_{ws}(\xi, \gamma) = \frac{4}{\pi} \left\{ \delta_w - \frac{1}{2} \tan^{-1}(2 \tan \delta_w) \right\}$$

$$\delta_w(\xi, \gamma) = \cos^{-1} \left\{ \frac{\gamma}{\bar{h}_V(\xi)} \right\} \quad \gamma < \bar{h}_V(\xi) < 1$$

The coefficients are defined $C_Y = Y/qA_r$ and $C_n = M_z/qA_r L$, with $A_r = \pi H_V^2/4$, L as the body length, and $\lambda = L/H_V$. The x coordinate

*The reference area $\pi H_V^2/2$ is employed in Reference 1, whereas $\pi H_V^2/4$ is used in the present report.

is directed along the vehicle axis rearward from the nose, and $\xi = x/H_V$. The station $\xi = \xi_1$ is located where $h_w = h_v$ on the forebody, and λ_1 designates the value of ξ at the rear end of the forebody, where $h_v' = 0$. The local height of the vehicle $h_v(x)$ is scaled with the maximum vehicle height H_V , giving $\bar{h}_v(\xi) = h_v/H_V$.

The method of reference 1 assumes that the fluid passes beyond the station of maximum height essentially moving parallel to the free stream flow, instead of following the body surface as it may close at the rear. This means that the pressure recovery is assumed to be negligible behind the maximum vehicle section. This assumption is in contrast to the method of reference 9 where closure of the flow is assumed where the body closes at the rear.

Viscous-Cross Flow Equations

Viscous-cross flow is included in reference 1 by adding the cross-flow effects to the slender-body effects giving

$$C_Y = \left\{ 8I_1(\gamma) + \frac{4}{\pi} k r_{wc}(\gamma) \int_0^{\beta\lambda} g(\sigma) d\sigma \right\} \beta \quad (4)$$

$$C_n = \frac{1}{2} C_Y - \frac{8}{\lambda} I_3(\gamma) \beta - \frac{4k r_{wc}(\gamma)}{\pi\lambda} \int_0^{\beta\lambda} \sigma g(\sigma) d\sigma \quad (5)$$

The viscous cross-flow effects are incorporated in the function $g(\sigma)$, plotted in Figure 2.3 of reference 1. The effect of the side rail is reflected in $r_{wc}(\gamma)$, plotted in Figure 2.5 of reference 1.

The empirical factor k is included to incorporate the effects of body cross-sectional configuration, nose profile and similar factors not represented in the cross-flow theory

presented in reference 2. In the present study recommendations on values of k will be made. For a missile-type body of revolution correlated in reference 2, the theoretical value of $k = 1.0$ is given.² For bodies with an elliptic cross section, data reported by Schindel⁵ indicate $k = 1.57$ according to reference 1.

In selecting a value of k for a high-speed ground vehicle, it should be recognized that, from an aerodynamic point of view, the "equivalent" body to a vehicle at the ground surface would include the vehicle and its image below the ground surface. For example, a vehicle with a half-circle cross section would have an equivalent body with a circular cross section.

A practical high-speed ground vehicle might have a cross section that is nearly square with a rounded top. In the absence of data for a specific cross section of this type, data for a 2:1 elliptic cross section might reasonably be taken as the equivalent body for engineering purposes.

3. CORRELATION OF EXPERIMENTAL DATA

3.1 GRUNWALD DATA OF NASA TN D-5935 (REFERENCE 3)

A series of force and moment tests was conducted with six unpowered, high speed-ground vehicle model configurations having various cross-sectional shapes. The tests were performed over the moving-belt ground plane in the 17-foot test section of the Langley 300-mph 7-ft by 10-ft tunnel and reported by Grunwald³.

A sketch of the axis system, force and moment designations of reference 3 is reproduced in Figure 2. The results presented here are for $\alpha = 0^\circ$ and the belt moving at the speed of the tunnel air. Model configurations are shown in Figure 3.

Scaling Factors

For scaling Y and M_z , references 1, 3 and 9 all employ the dynamic pressure of the resultant flow, $v_r = (V^2 + v_c^2)^{1/2}$, where V is the vehicle velocity and v_c is the velocity of the side wind. In wind-tunnel tests where the body is yawed to simulate a side wind, as in reference 3, v_r is the free-stream velocity. The force and moment data presented in reference 3 use the maximum cross-sectional area of the body, A_m , for scaling, giving a side-force coefficient $\bar{C}_Y = Y/q A_m$. The yawing-moment data presented in reference 3 are scaled with L , giving $\bar{C}_n = M_z/qA_m L$.

Scaled on this basis, the \bar{C}_Y data of Grunwald³ at $\beta = 20^\circ$ are plotted in Figure 4a for all models as a function of the nondimensional gap height, H/d_e , where d_e is the diameter of a circle with cross-sectional area equivalent to maximum cross-sectional area of model. The \bar{C}_Y data for the various configurations have a relatively small spread at $H/d_e = 3.7$, but at smaller H/d_e the spread is considerable. The models with the flat lower surfaces have the smaller \bar{C}_Y values.

The moment data of Grunwald³ are plotted in Figure 4b. The spread in \bar{C}_n is large on a percentage basis at all values of H/d_e .

The side-force and yawing-moment data of Grunwald³ scaled in terms of the area $A_r = \pi H_v^2/4$ are plotted in Figure 5 where $C_y = Y/qA_r$ and $C_n = M_z/qA_r L$. The C_y data in Figure 5a collapse together fairly well as H/d_e goes to zero and are relatively independent of H/d_e for $H/d_e < 0.1$. The C_n data in Figure 5b have a smaller spread at low H/d_e values than in Figure 4b, although the improvement is not as good as achieved in the side-force data. At small H/d_e values the C_n data for the square-type model deviate the most from the group. In fact, the rising trend in C_n as H/d_e is reduced, is quite marked. The C_n data for all other models is fairly independent of H/d_e below 0.1.

The side force and yawing moment, therefore, will be correlated through the remainder of this study using $A_r = \pi H_v^2/4$ as the reference area.

Half Circle-Cross Section Model

The variation of C_y and C_n with side-slip angle θ is presented in Figure 6 for the half circle-cross section configuration of Grunwald³. The variations are linear within the data scatter up to about 14° . Allowing for an offset in the zero side-slip angle of about $-1/2$ degree, the C_y data fall about 20 percent above the slender-body predictions of Woolard⁹, Equation (1), and Ruetenik and Zartarian³, Equation (2), in the linear range; the C_n data, on the other hand, lie about 45 percent below the slender-body curve given by Equation (3).

Going back to the correlation made in reference 2 of this nonlinear theory with bodies of revolution, where no ground plane is present, it is found that the linear range of the normal force and pitching moment about the vertex with angle of attack is much smaller, being only about 5 degrees, and that the data agree well with the nonlinear theory for $k = 1.0$ up to 20° and more.

An examination of the distribution of the section normal force along an ogive-cylinder body correlated in reference 2 shows that the loading agrees with slender-body theory on the forebody from the nose to the point where the slender-body theory predicts a maximum, but the loading falls off more slowly rearward. This would explain C_Y being larger than predicted by slender-body theory; but then C_n would also be greater than predicted by slender-body theory, whereas the values are found to be lower.

It appears that the strength of the leeward vortices affords the only explanation. A greater vortex strength on the ground-vehicle model than on the bodies of revolution used in the wind-tunnel tests correlated in reference 2 would show up as an increase in side force, and at small angles of sideslip the vortex loading is expected to increase in the rearward direction, leading to a reduction in the yawing moment. There is no clear explanation why the vortex strength might be greater, but it could be associated with the moving ground plane. This question might be cleared up for the moving ground plane experiments by making measurements on models of the local pressure.

The appropriate value of k for a ground vehicle with a half circle-cross section configuration, on the basis of the discussion in Section 2.2, would be $k = 1.0$. The C_Y data do not follow the rapid increase with β beginning at about 8° indicated by Equation (4) for $k = 1.0$. The slower rise in the C_Y data would match the theory at 20 degrees with $k = 0.3$.

This slower rise in C_Y with β than expected from the wind-tunnel results could be explained also by the ground plane. When the leeward vortices become large relative to the size of the body, the ground plane could inhibit their further growth. This effect has been observed elsewhere, and will be discussed further below. For the present, it is sufficient to note that

inhibiting the vortex growth would explain both the departure in the C_Y and C_n data from the respective curves for $k = 1.0$ at the higher values of β .

It is concluded then that the large linear extent of C_Y and C_n data in terms of β does not imply the absence of viscous effects to such large angles as 14 degrees, but that the ground plane may control the viscous effects in such a way as to result in linear variations. This result focuses attention on the question of ground-plane simulation.

Square Type-Cross Section Model

The C_Y and C_n data for the square-type model are compared in Figure 7. The data appear to indicate a zero-side slip angle of $+1/2^\circ$. The data agree with the slender-body curves of Equations (1) and (2) in the range $\beta < 5^\circ$. For $\beta > 5^\circ$, the data are about 15 percent above the slender-body value of Equation (1) and 10 percent above Equation (2) up to 12 degrees. Beyond 12 degrees the deviation increases with β .

It is difficult to define a nonlinear range, but it would appear that vortex effects may exist at $\beta \geq 6^\circ$. For the nonlinear range, a value of $k = 1.57$ would be expected following the discussion of Section 2.2. The C_Y data agree fairly well with Equation (4) for $k = 1.57$, although the values are clearly high relative to the $k = 1.57$ curve in the range $5^\circ < \beta < 10^\circ$ and fall progressively below a constant- k curve for increasing β , as did the data for the half circle-cross section model. At $\beta = 20^\circ$, a value of $k = 0.75$ would match the theory to the data.

The C_n data, allowing for the $+1^\circ$ offset in the zero-side slip angle, are linear within the data scatter over the entire range, and fall about 25 percent below the slender-body value for Equation (5).

Circular-Cross Section Model

The C_Y and C_n data from the circular-cross section model are compared in Figure 8. Allowing for a zero sideslip angle of +1 degree, the C_Y values compare with the theoretical predictions in about the same way as for the square-type cross section. For $\beta < 5^\circ$, the data agree with the slender-body value of Equation (2). The data are significantly above the curve in the range $\beta > 5^\circ$.

For engineering purposes, Equation (4) for $k = 1.57$ could provide a reasonable approximation to the data. However, the data tend to be higher in the range $5^\circ < \beta < 10^\circ$, and to fall progressively lower relative to a constant-k curve as β increases. At 20 degrees, the data would match Equation (4) for $k = 0.8$.

The C_n data are essentially linear in β over the full range and about 35 percent below the slender-body curve.

Ground Plane

The ground surface could have two effects on the air loads produced on a ground vehicle by a side wind. First, a boundary layer would be present near the ground tending to cause the flow to separate on the windward side of the vehicle, resulting in lower pressures on the windward side. This boundary layer would not be present with a moving-belt facility where the belt is aligned with the tunnel flow, such as employed in reference 3.

Secondly, the moving ground plane on the leeward side of the body may tend to induce vortex formation on the leeward side at small angles of sideslip, resulting in higher C_Y values, as observed for the half-circle and square-type models. Yet the same ground plane could impede the growth of the leeward vortices when they become large, as at high sideslip angles.

A demonstration of the influence of a surface in a similar situation is shown in Figure 9, from experiments performed by Roshko¹⁰. A circular cylinder was mounted crosswise in a wind tunnel and a splitter plate was placed downstream in the wake as shown in Figure 9a, where the flow is from the left. The pressure distribution in the wake is shown in Figure 9a. The splitter plate increases the downstream recovery in pressure, reducing the drag in this case.

The pressure distribution around the cylinder of reference 10 is shown in Figure 9b. The pressure recovery on the back side is clearly much greater with the splitter plate. The effect of the plate is to reduce the drag coefficient in this case from 1.15 to 0.72. For the Reynolds number of these data, the flow would be subcritical, but the effect would be similar if it were supercritical.

Whether the windward and leeward effects with the moving-belt ground plane would be the same as for a high-speed ground vehicle remains to be determined.

Discussion

From these results it is concluded that C_y for a ground vehicle would be the same as predicted by slender-body theory for $\beta < 5^\circ$. The departure from the slender-body value for $\beta > 5^\circ$ depends upon the cross section and sideslip angle.

For engineering purposes, Equation (4) would appear to give useful estimates of C_y to $\beta = 20^\circ$. For a high-speed ground vehicle typified by the square type-cross sectional configuration, Equation (4) would be used with $k = 1.57$. It is expected most vehicles would more nearly approximate a square-type cross section. Similarly, C_n might be estimated as 55 to 75 percent of the value given by Equation(3) for $k=0$, depending upon the configuration of the cross section. For a half-circle

cross section C_n would be taken as 55 percent of the Equation (3) value for $k=0$, for a square-type cross section as 75 percent, and for a circular cross section as 65 percent.

3.2 GRUNWALD DATA OF NASA TN D-6011 (REFERENCE 6)

A series of force and moment tests was conducted with unpowered, high speed-ground vehicle models having the configurations shown in Figure 10. A rectangular-type model is shown in Figure 10a, a side-by-side model with a flat-bottom configuration in Figure 10b and a side-by-side model with a contoured-channel configuration in Figure 10c. Two air cushions were tested in the rectangular model, a peripheral-jet cushion and a modified plenum cushion. The objective of the present study is to determine whether the results for air cushions are similar to the results for air gaps discussed above.

The C_Y and C_n data for the rectangular body are plotted in Figure 11. The C_Y data in Figure 11a indicate a zero-sideslip angle of about +2 degrees. Equation (1) predicts a zero side force because the body closes at the rear. For $\beta < 20^\circ$, the data follow the trend observed for the solid models examined in Section 3.1. At $\beta = 10^\circ$, the C_Y values are about 20 percent above the slender-body curve of Equation (2). At $\beta = 10^\circ$, the data match Equation (2) for $k = 1.57$ fairly well, and progressively fall below the $k = 1.57$ -curve as β increases, similar to the trend for the square-type cross section.

The C_n data at $\beta = 10^\circ$ fall within the experimental scatter of the expected value, which is 25 percent below the prediction of the slender-body curve of Equation (3). At higher β values, C_n falls off somewhat further from the slender-body curve, lying between the $k = 1$ and $k = 1.57$ curves.

The correlation of the data for the side-by-side configuration in Figure 12 is similar to the rectangular-body results, although the data spread is greater.

It is concluded that C_Y and C_n results for the air-cushion models are in agreement with the results for the rigid models with an air gap to the ground plane discussed in Section 3.1.

3.3 TRACKED HOVERCRAFT LIMITED DATA OF FRA-RT-71-68 (REFERENCE 7)

Tracked Hovercraft Limited⁷ (THL) reported a series of wind-tunnel experiments studying the forces and moments for two design concepts of a high-speed ground vehicle.

The side view of the two basic models is sketched in Figure 13, showing the model profiles and track system. The upper model is configured for an inverted-tee track and the lower model for a channel track. Two aft configurations were employed. Both aft configurations closed at the rear, but one was symmetrical with the forebody configuration and one was asymmetric.

The tracks extend ahead and behind the vehicle models. A strip of abrasive was attached to the models along the line identified as "transition" to promote turbulent transition of the cross flow over the model for better simulation of the full-scale situation. The model on the track is yawed in the wind-tunnel tests to simulate a side wind.

The cross section of the two models and the associated tracks are shown in Figure 14. The cross sections are basically rectangular with a semi-circular top. The track base has a rectangular cross section (instead of a ground plane) characterizing an elevated track section.

Inverted-Tee Configuration

The side-force and yawing-moment data are plotted in Figure 15, as taken from Reference 7. Equation (1) from Woolard⁹ predicts a zero side force for this model because of model closure at the rear. The solid line in the upper graph represents the slender-body prediction, Equation (2). At $\beta = 3^\circ$ the C_Y data agrees with

the slender-body prediction. Up to 10 degrees, the data agree with Equation (4) for $k = 1.57$, the value proposed in Section 2 for a high-speed ground vehicle with a square-type cross section. Beyond 10 degrees the C_Y data fall away from the $k = 1.57$ curve, matching a value of $k = 0.6$ at 20 degrees.

The C_n data agree with the slender-body prediction at $\beta = 3^\circ$, and fall about 15 percent below the prediction at higher values of β .

For C_Y these results are quite similar to the results for the square type-cross section model, Figure 7. The C_n values comparatively are somewhat higher, being only 15 percent below the slender-body curve, compared with 25 percent for the square type-cross section model. The comparatively higher C_n values for the inverted-tee configuration could indicate partial recovery of the flow at the rear; the effect, even with this complete body closure, is relatively small, so for engineering purposes body closure at the rear could be neglected for the inverted-tee configuration.

The relatively good agreement between these results for an inverted-tee model on an elevated guideway and the solid model with a square-type cross section above a moving-belt ground plane would indicate the following. Either the effect of the ground plane on the leeward vortices is considerably smaller than would be deduced from the experiments of Roshko¹⁰, as discussed in Section 3.1, or else the inverted-tee center rail has an effect on the loading similar to the ground-plane effect. This question might be resolved by measurements of the pressure distribution on the body, or by experiments in which the ground plane and the center rail are added successively in separate tests.

For the time being, it is reasonable to assume that the results of the tests with a ground plane reported in reference 3, and discussed in Section 3.1, would apply to an inverted-tee guideway.

Channel Configuration

The data from the channel tests of Reference 7 are reproduced in Figure 16. The C_Y values are essentially zero for $\beta < 15^\circ$, and rise thereon in a nonlinear fashion. They are less than the slender-body values of Equation (2) for $\beta < 20^\circ$. Equation (1) from Woolard predicts $C_Y = 0$ because of model closure at the rear. The reduction in C_Y by this side-rail height of $\gamma = 0.43$ is much greater than predicted by Equation (4) for the vortex theory, even with k as small as 1.0.

The C_n values, on the other hand, are about double the slender-body prediction of Equation (3). Any nonlinear trend is small.

These two results, (1) $C_Y = 0$, and (2) C_n double the value for a cutoff tail, indicate that closure at the rear appears to be effective with a side rail. The effect of closure on a body according to slender-body theory is to apply a side force equal and opposite to the side force effective on the forebody, thereby eliminating the side force and doubling the yawing moment, which is the result observed here.

The effect of the side rail is significant to the design of a lateral constraint system. First, the side force and moment are reduced by blockage from the side rail. Secondly, the side rail blockage appears to make closure of the body at the rear effective in essentially eliminating the side force. Elimination of the side force by model closure would not necessarily reduce the forces on the lateral constraint, because the moment would have to be opposed, but the mean lateral acceleration on the vehicle due to the wind would be eliminated. Also, the nonlinear component of the side force is appreciably lower than expected, which indicates that the side rail may significantly reduce the growth of the leeward vortices.

3.4 GRUMMAN TACRV DATA (REFERENCE 8)

Grumman⁸ has reported a series of force and moment measurements carried out in a wind tunnel with the model of the Tracked Air Cushion Research Vehicle (TACRV) shown in Figure 17. The model has side rails and simulated air cushions, and in addition has a jet propulsion nacelle mounted on the top of the body to the rear. The model is 1/10th scale of the TACRV.

The guideway is elevated. There is an air gap along the bottom of the side rail. The side rail extends ahead and behind the model, as in the THL⁷ tests. The model system is yawed to simulate a side wind.

The measured side-force and yawing moment data of reference 8 are presented in Figure 18, where the measured data have been adjusted for the static tare values of the side force and yawing moment measured with the cushion air on and the tunnel air off.

Four of the curves plotted in Figure 18a are based on the vehicle without the engine nacelle. This assumes that the flow-through nacelles used in most of the tests do not influence the lateral forces due to wind. Specifically H_v is taken as 10.25 in., the height to the top of the cab.

Over this limited range of β ($\beta < 12^\circ$), all of the curves are in fairly good agreement with the C_y data, within the data scatter. The value of $k = 1.57$ recommended for a square-type cross section from the data of Section 3.1 - 3.2 provides a good estimate over the limited range.

The long-dash curve represents C_y where the engine nacelles are included in the aerodynamic model. It is assumed in this case that the side force increases with the square of the vehicle height so H_v is taken equal to the vehicle height to the top of the engine nacelles, 14.25 in. This comparison shows that neglecting the presence of the nacelles in determining the aerodynamic model provides a considerably better estimate of C_y .

The C_n data are compared in Figure 18b. Here the C_n values are much overestimated using Equation (3) or Equation (5) for either $k = 1.0$ or 1.57 neglecting the engine nacelles. On the other hand, inclusion of the engine nacelles in the aerodynamic model in the manner described above for C_y considerably overestimates the moment in the opposite direction.

It is possible that the force on the forebody is less than estimated using Equation (2) and that the force on the nacelles makes up the difference in such a way as to match the predictions of Equation (4) for C_y in Figure 18a and result in a nearly-zero yawing moment, as indicated in Figure 18b. This question cannot be resolved on the basis of the data available from the tests described here. It would be necessary to systematically vary the model and track configurations and study the incremental effects when components are added or removed. In particular, it would be worthwhile to measure forces on individual components and local pressures.

4. CONCLUSIONS

Based on the analysis of laboratory test data analyzed here for determining the effect of steady side winds on the side force and yawing moment for tracked air-cushion vehicles, the following conclusions are reached.

1. For unpowered TACV bodies mounted in close proximity to the surface in a moving-ground plane facility, the variation of the side-force coefficient, C_Y , with side-slip angle; β , falls into two patterns: one pattern for cross sections with a half-circle configuration and another pattern for cross sections with a square-type or circular configuration. For TACV, which generally would be better approximated by a square-type cross section, slender-body equations, Equations (1) and (2) correlate for $\beta < 5^\circ$ and the viscous-cross flow method, Equation (4) with $k = 1.57$, shows fair correlation to $\beta = 20^\circ$, although C_Y does not increase as rapidly with β as the method predicts. The viscous-cross flow method is based on wind-tunnel results for bodies without a ground plane, and the departure from the method at large β is tentatively attributed to constraint on lee vortex growth by the ground plane, although some question remains regarding ground-plane simulation.
2. For the unpowered TACV bodies, the yawing moment, C_n , varies linearly with β to about 20 degrees, but it is 15 to 35 percent less than predicted by slender-body theory, Equation (5). The viscous-cross flow theory based on wind-tunnel results, Equation (5), is inadequate for predicting C_n .
3. For the powered air-cushion models, the variations of C_Y and C_n with β are essentially similar to the variations for the unpowered TACV bodies.

4. For unpowered TACV bodies on an elevated inverted-tee guideway, the variations of C_Y and C_n with β are similar to the variations for the surface TACV bodies in the moving-ground plane facility. Body closure at the rear has a relatively small effect on C_Y and C_n in this situation.
5. For the elevated channel guideway, body closure at the rear of the vehicle has a marked influence aerodynamically. As predicted by slender-body theory for a body with closure, C_Y is negligible for $\beta < 16^\circ$ and C_n is double the value for a body with a cutoff base. The absence of side force implies very little rolling moment, which may be of even greater significance. With side rails the nonlinear effect is significantly less than predicted by the viscous-cross flow theory.
6. Verification is needed for the side-wind problem of the simulation achieved using either a moving ground plane or fixed ground plane in a wind tunnel for high-speed ground vehicles on fixed guideways.
7. Systematic tests are needed for various vehicle configurations on the effect of side rails.

APPENDIX
MEASUREMENT OF SIDE FORCE ON FULL-SCALE TACV
DUE TO SIDE WIND

The determination of side forces for high-speed ground vehicles due to side winds by measurements carried out on models in wind-tunnel tests can be useful for design purposes. But, until wind tunnel simulation has been verified for high-speed ground vehicles, it would be desirable, and perhaps should be an engineering requirement, to confirm the measurements through tests in the field. The objective of this appendix is to present calculations for examining the practicability of making such measurements.

The tests performed by Grunwald⁶ indicate that C_y and C_n for an air-cushion vehicle are essentially independent of the dynamic-pressure ratio $q A_c/L$, where A_c is the planform area of the air cushion and L is the static lift. This means that under conditions of low wind speed tests could be run at a low vehicle speed to achieve the sideslip angles of interest for high vehicle speeds.

In Colorado, where tests might be performed, winds of 30 mph could be taken as a design condition for testing, so aerodynamic conditions corresponding to a wind of 60 mph for a vehicle traveling at 150 mph could be simulated at a vehicle speed of 75 mph. A sketch of the test arrangement considered here is shown in Figure 19. A barrier would be positioned to shield the vehicle from the side wind. The barrier would be long enough for lateral motion of the vehicle that is produced before the vehicle reaches the barrier to die out. The barrier would probably have a roof extending over the track to prevent a wake from forming at the guideway.

A test vehicle is postulated for these sample calculations having the following characteristics:

Length: 91.7 ft
 Height: 11.0 ft
 λ : 8.33
 Weight: 60,000 lbs
 Speed: 75 mph

For this vehicle, the equations of reference 1 give

$$C_Y = C_{Y_S} + C_{Y_C}$$

$$= (4 + 4.80)0.38 = 3.34$$

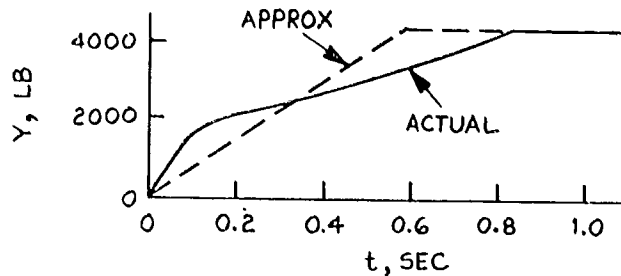
where $\beta = 0.38$ rad. The steady-state side force for these conditions is

$$Y = C_Y \frac{\pi H^2}{4} \frac{1}{2} \rho V^2$$

$$= 3.34 (95 \text{ ft}^2) 14.2 \text{ psf}$$

$$= 4500^\#$$

The side force would grow about as shown by the solid line shown in the sketch. When the vehicle reaches the end of the barrier, the slender-body side force on the nose would rapidly grow to the



steady-state value of about 2000[#]. The viscous forces develop more slowly, reaching a steady state when the vehicle emerges completely behind the barrier. The loads would reach the steady-state value then in about 91.7 ft/110 fps = 0.83 seconds. For the present analysis, the side force is approximated as a 0.6-second ramp, as shown in the sketch by the broken line.

The secondary suspension of the vehicle is taken as a single-degree-of-freedom system having a natural frequency of 0.8 Hz, from the TACV systems study carried out by TRW, reference 11. The maximum acceleration of this system, neglecting damping, would occur at $t = 0.925$ seconds. The maximum acceleration would be

$$\begin{aligned} \ddot{y}_{\max} &= \frac{Y_{\max}}{k} \frac{2\pi f_n}{t_0} \left[\sin\left(\frac{2\pi t}{T} - \frac{2\pi t_0}{T}\right) - \sin\frac{2\pi t}{T} \right] \\ &= \frac{4500^{\#}}{3920^{\#}/\text{in.}} \frac{2\pi \cdot 0.8}{0.6} \left[\sin\left(\frac{0.925 - 0.6}{1.25}\right) 2\pi - \sin\frac{2\pi \cdot 0.925}{1.25} \right] \\ &= 19.2 \text{ in/sec}^2 = 0.050 \text{ g's} \end{aligned}$$

where t_0 is the ramp time of 0.6 seconds and $k = (W/g)(2\pi f_n)^{1/2} = (60,000/386.4)(2\pi \cdot 0.8)^{1/2} = 3920$ ppi.

The passenger compartment is also subjected to lateral accelerations caused by irregularities in the guideway. Taking 0.01 g's rms as this lateral acceleration of the passenger compartment due to the guideway, the 0.050 g's due to the side wind would be measureable, but the accuracy would be low.

The wind force could be measured with much greater accuracy by compensating for the acceleration due to the track. The lateral acceleration due to track roughness could be subtracted from the measured acceleration of the passenger compartment by measuring the pressure in the air cushions through which the track acts. On the basis of the single-degree-of-freedom system, representation of the lateral motion of the passenger compartment, the following equation applies

$$m\ddot{y} = Y + Y_{\text{cushions}}$$

where m is the mass of the vehicle, \ddot{y} is the lateral acceleration, Y is the force due to the side wind, and Y_{cushions} is the net side force due to the air cushions. By measuring the acceleration

and applying the compensation for the cushion forces, the force due to the side wind should be measurable to an accuracy significantly better than the 0.01 g's.

In carrying out the measurements, the roll and yaw degrees of freedom would need to be accounted for, as well, perhaps, as elastic degrees of freedom. But the method is essentially straight forward, and can be checked by simple tests such as displacing the vehicle sideways and releasing when the wind velocity is zero.

6. REFERENCES

1. Ruetenik, J. R., and Zartarian, G., Development of Methods for Predicting Airloads on TACV Configurations Due to Strong Cross-Wind Gusts, Kaman Sciences Corp., Kaman Avidyne Div., Report KA-TR-76, March 27, 1972.
2. Ruetenik, J. R., and Brooks, W. B., Transient Airloads on a Body of Revolution Due to Indicial Sinking at a Large Angle of Attack, MIT, ASRL TR 121-1, August 1964.
3. Grunwald, K. J., Aerodynamic Characteristics of Vehicle Bodies at Crosswind Conditions in Ground Proximity, NASA TN D-5935, August 1970.
4. Perkins, E. W., and Jorgenson, L. H., Comparison of Experimental and Theoretical Normal-Force Distributions (including Reynolds Number effects) on an Ogive-Cylinder Body at Mach Number 1.98, NACA TN 3716, 1956.
5. Schindel, L. H., and Chamberlain, T. E., Vortex Separation on Slender Bodies of Elliptic Cross Section, MIT Aerophysics Laboratory, Tech. Report 138, August 1967.
6. Grunwald, K. J., and Johnson, W. G., Jr., Aerodynamic Characteristics of Air-Cushion Models at Very Low Ground Clearances and at Free-Stream Dynamic Pressures Exceeding Cushion Pressure, NASA TN D-6011, October 1970.
7. Tracked Hovercraft Limited, A Cost Comparison of Three Tracked Air Cushion Vehicle Configurations, Prepared for DOT Report PB 197501, July 1970.
8. Savaterri, C., Tracked Air Cushion Research Vehicle Aerodynamic Analysis, Grumman Aerospace Corp., Prepared for DOT Report PMT-B4-R71-06, March 1971.
9. Woolard, Henry W., Slender-Body Aerodynamics for High-Speed Ground Vehicles, Journal of Aircraft, pp. 597 - 602, August 1971.

10. Roshko, A., On the Drag and Shedding Frequency of Two-Dimensional Bluff Bodies, Calif. Inst. of Tech., NACA Report TN 3169, July 1954.
11. TRW HSGT Systems Eng. Study, Tracked Air Cushion. Prepared for DOT PB 190939. December 1969.

7. FIGURES

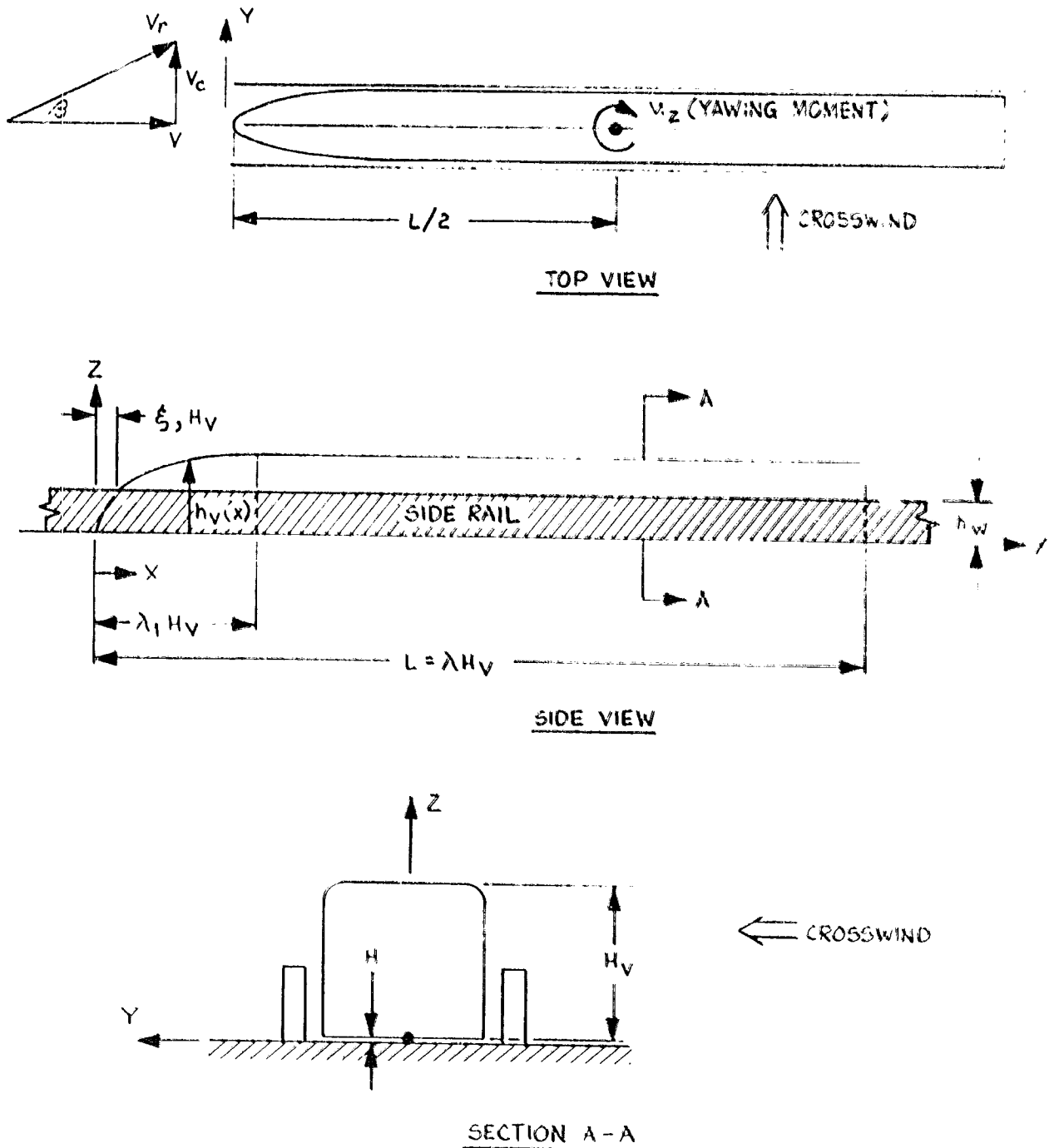


Figure 1 - Sketch of Representative Vehicle Constructed for Basis of Analysis.

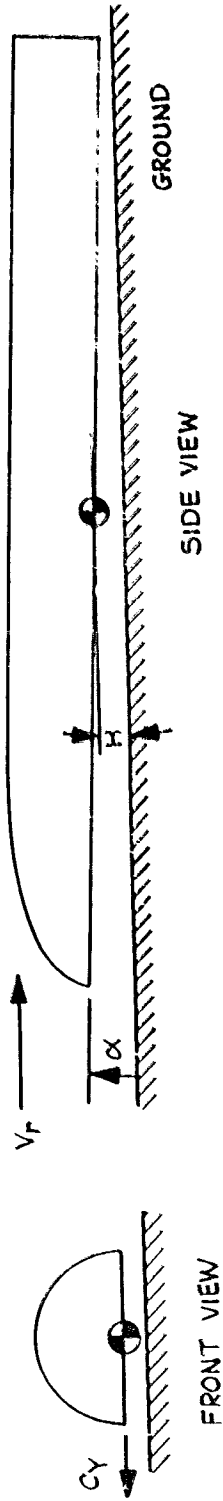
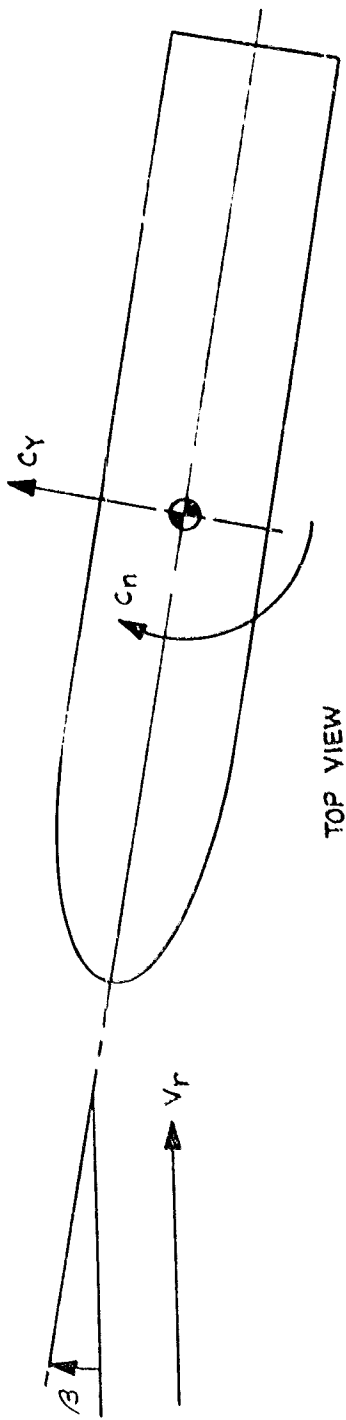
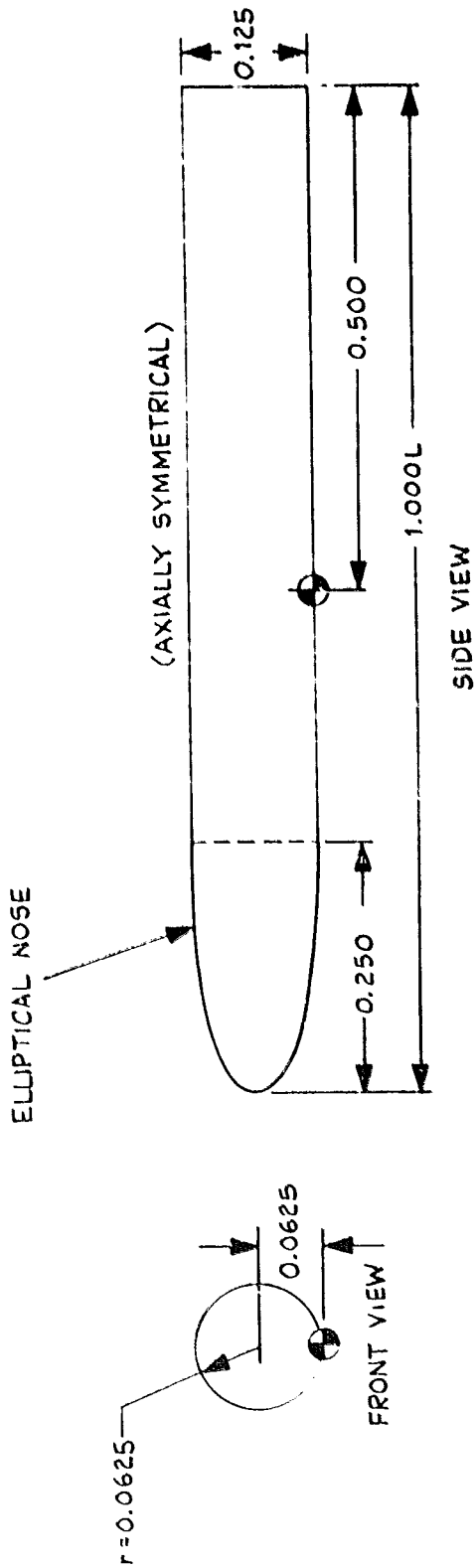


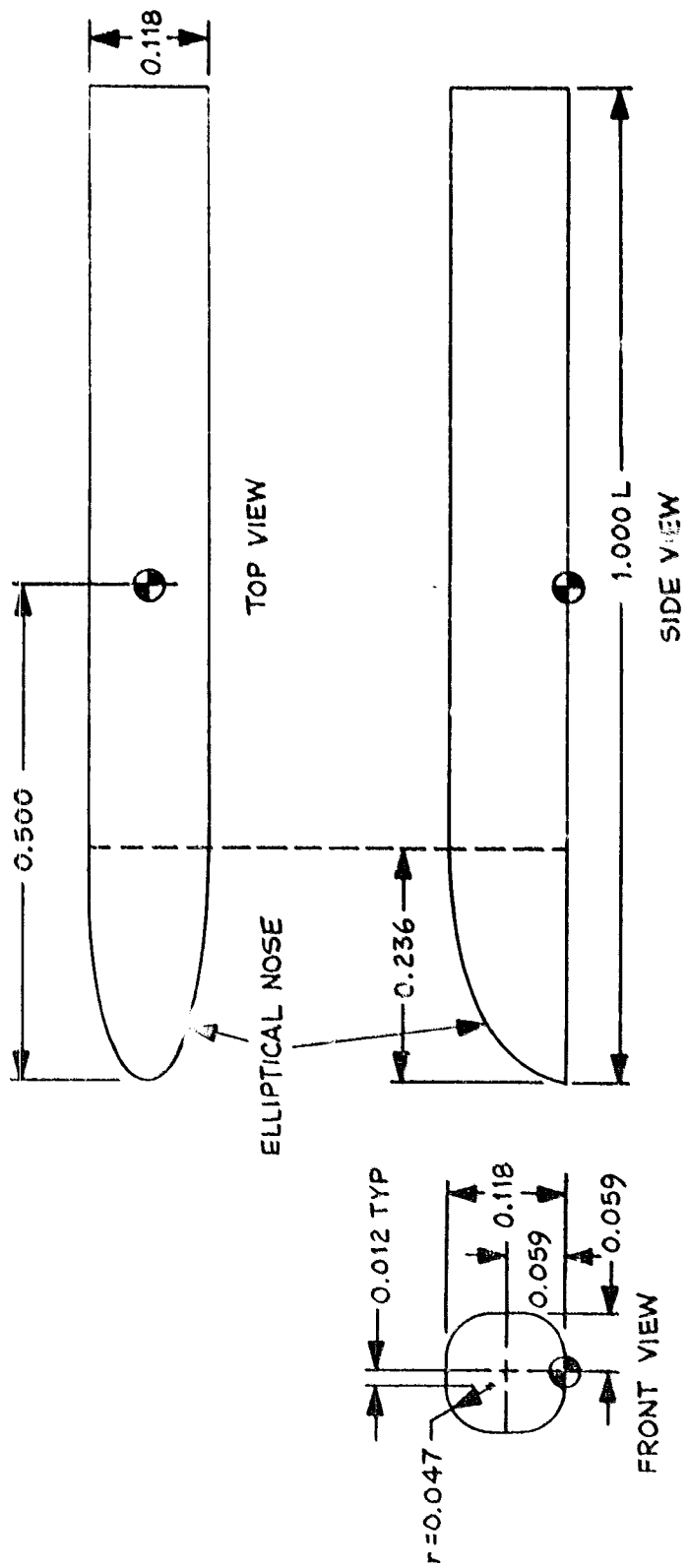
Figure 2 - Drawing of Axis System Showing Positive Direction of Forces, Moments, and Angles, NASA TN D-5935.



● MOMENT REFERENCE CENTER

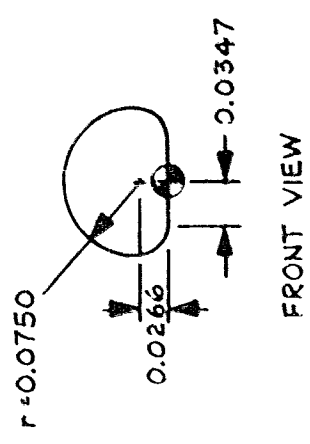
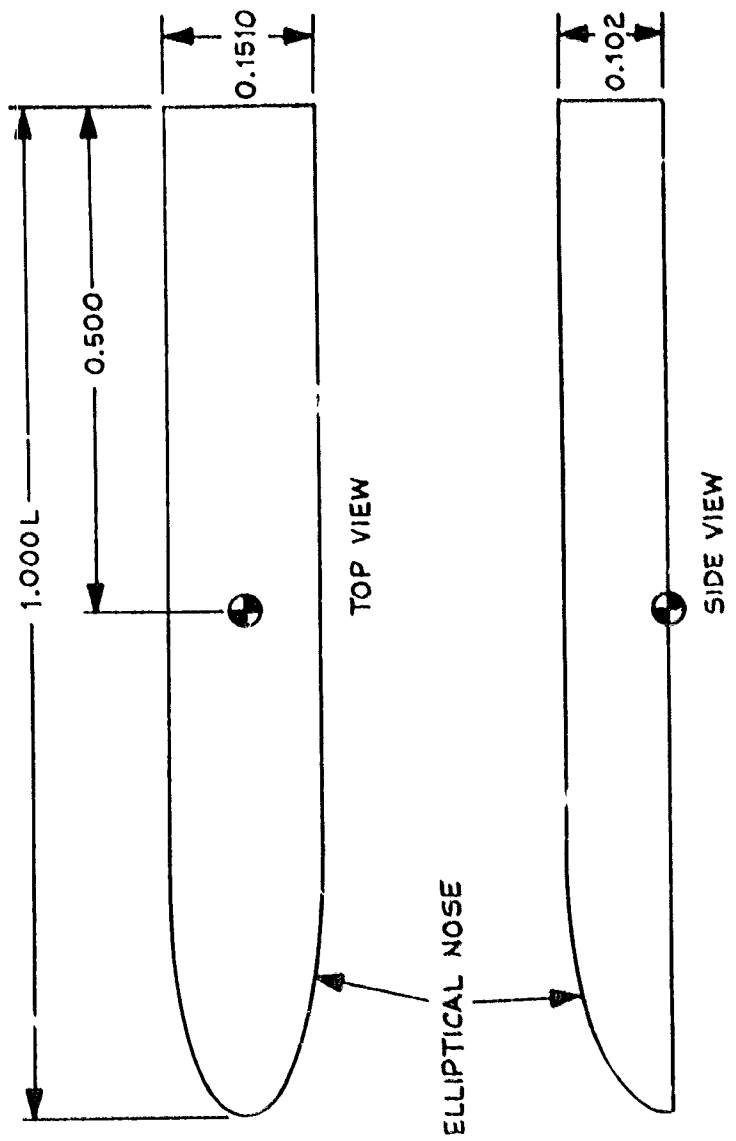
(a) CIRCULAR CROSS-SECTION

Figure 3 - Configuration of Six Models Employed in Tests by Grunwald, NASA TN D-5935.



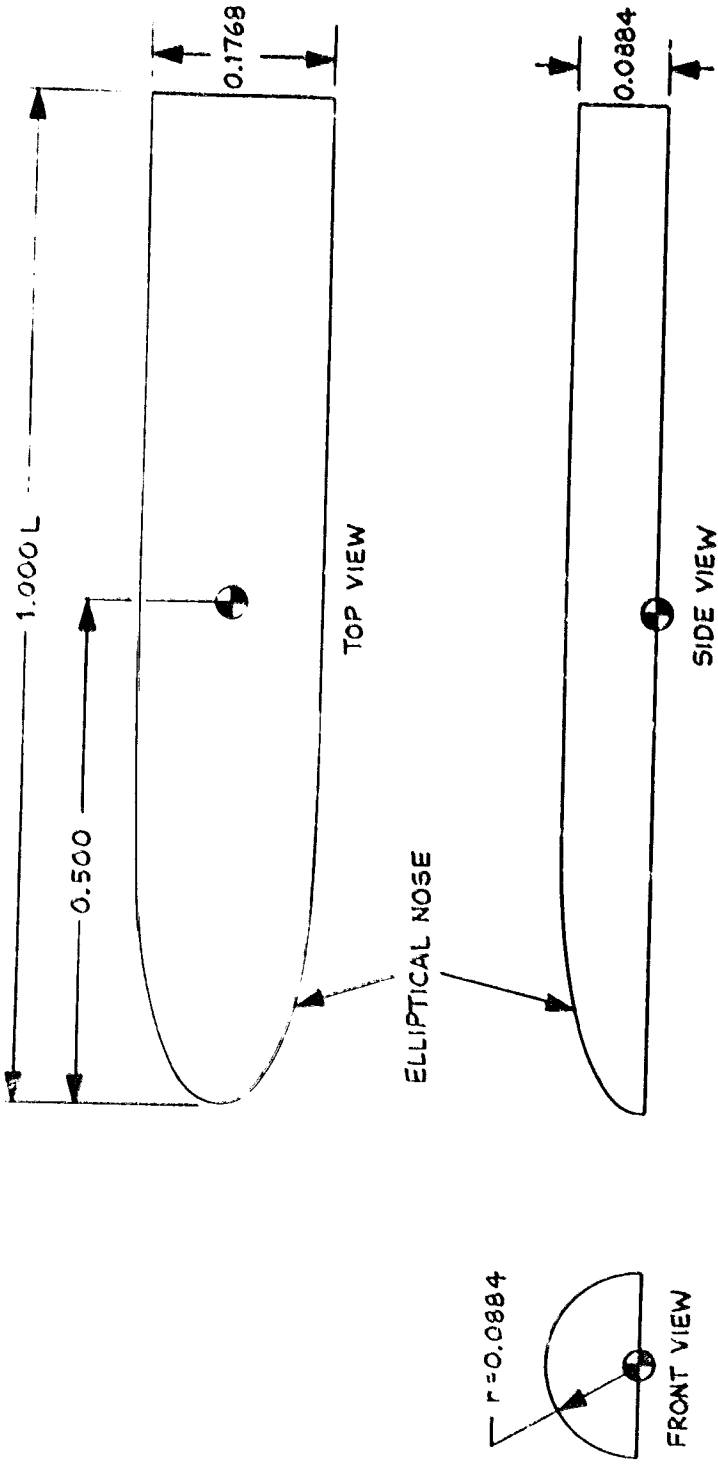
(b) SQUARE-TYPE CROSS-SECTION

Figure 3 - (Continued)



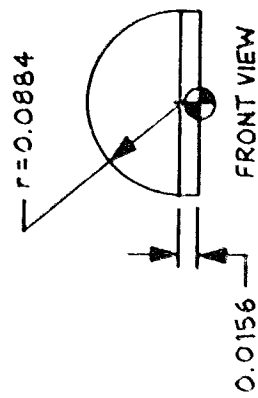
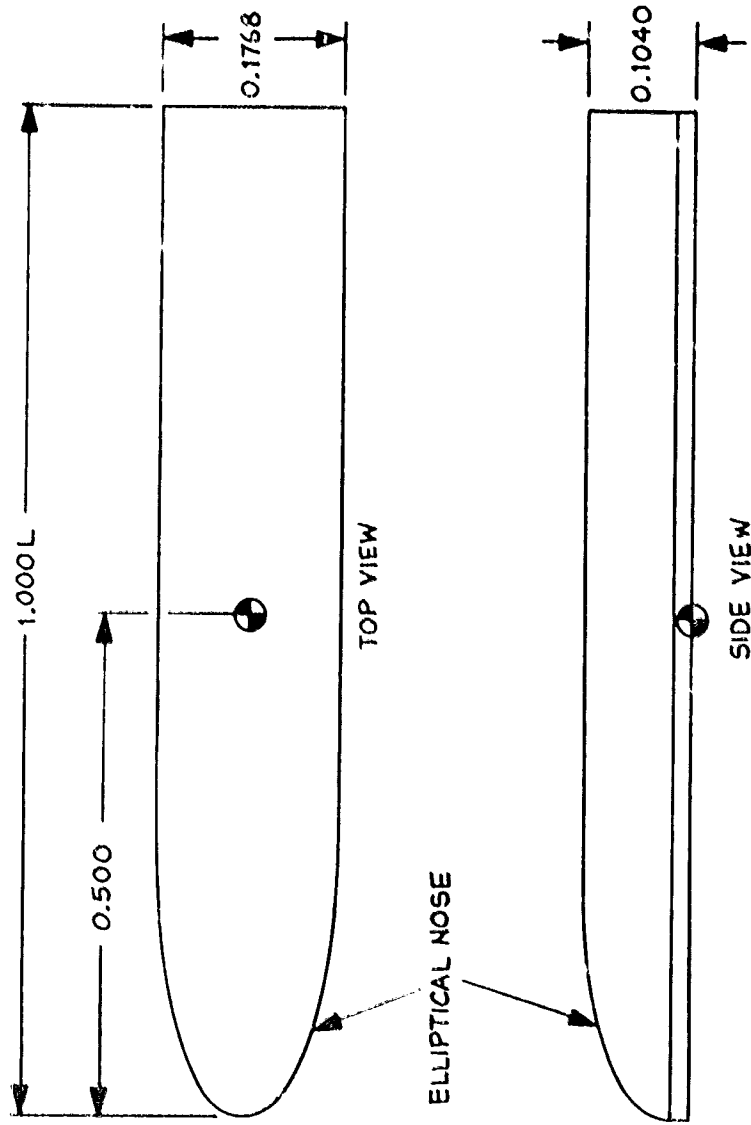
(c) TRIANGULAR-TYPE CROSS-SECTION

Figure 3 - (Continued)



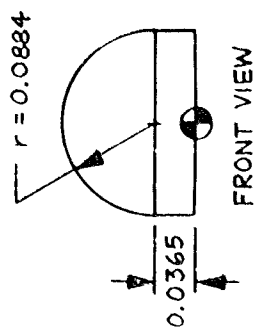
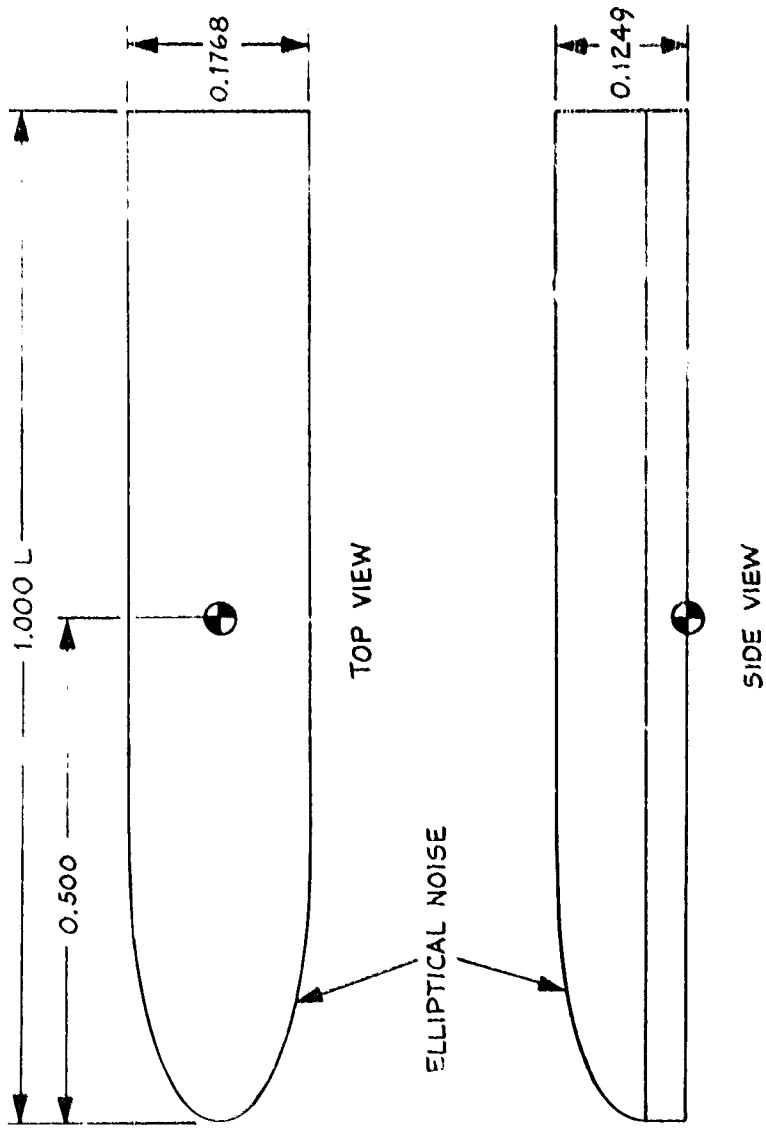
(d) HALF-CIRCLE CROSS-SECTION

Figure 3 - (Continued)



(e) HALF-CIRCLE (SHORT EXTENDED SIDES) CROSS-SECTION

Figure 3 - (Continued)



(f) HALF-CIRCLE (LONG EXTENDED SIDES) CROSS-SECTION

Figure 3 - (Concluded)

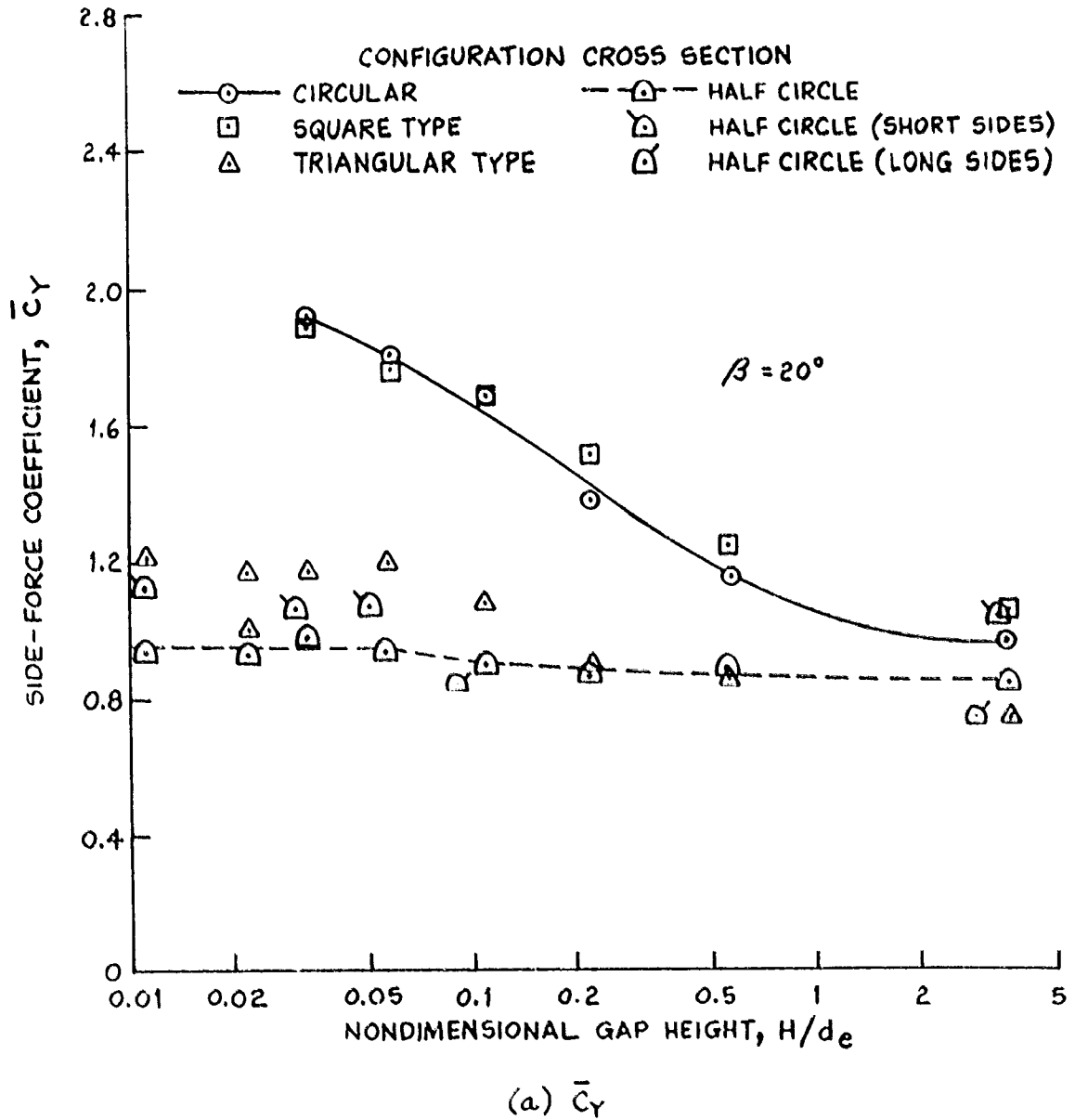
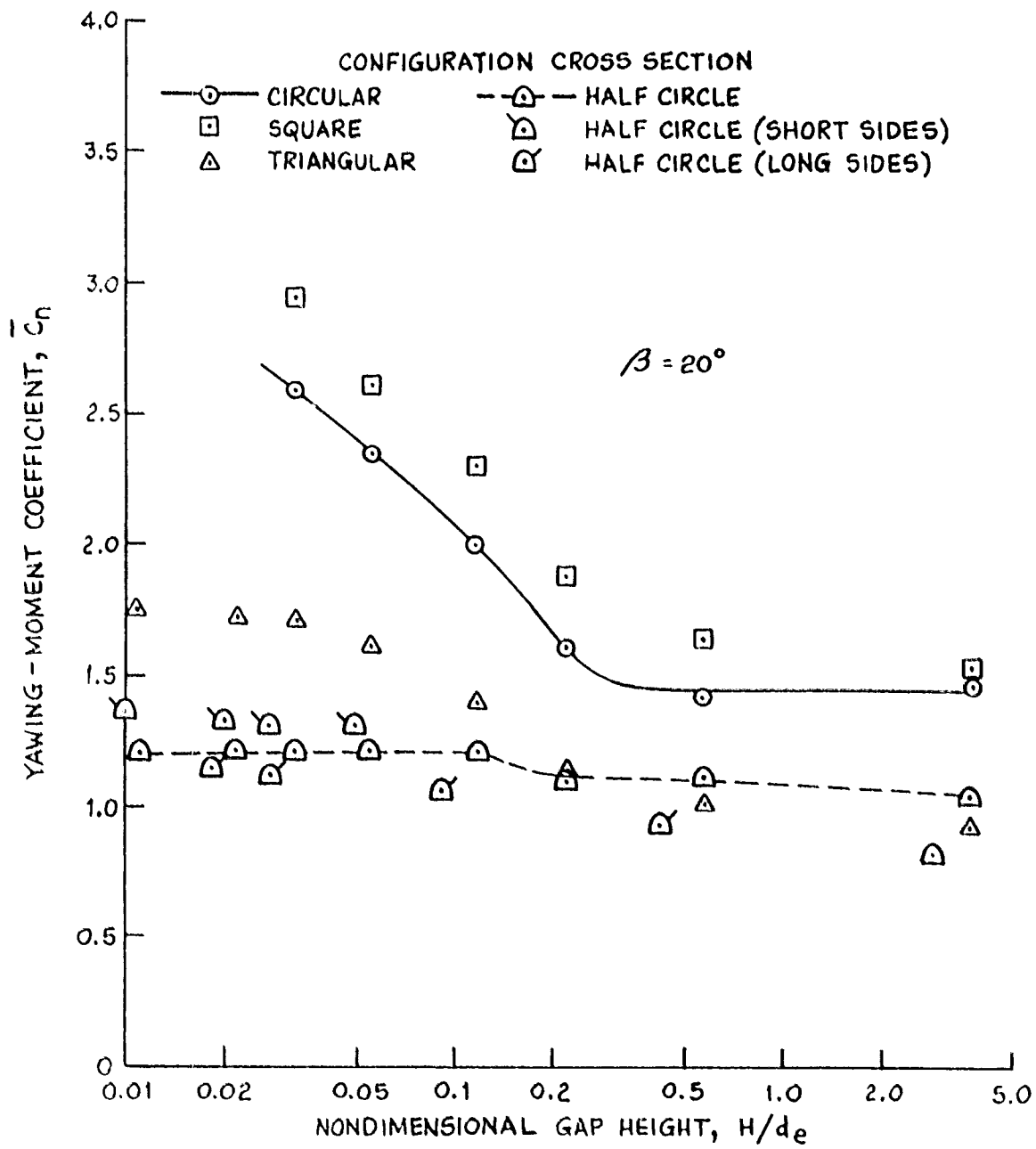


Figure 4 - Aerodynamic Coefficient Based on Maximum Cross-Sectional Area as a Function of Gap Height Above Ground Plane for Six Configurations Tested by Grunwald, NASA TN D-5935.



(b) \bar{C}_n

Figure 4 - (Concluded)

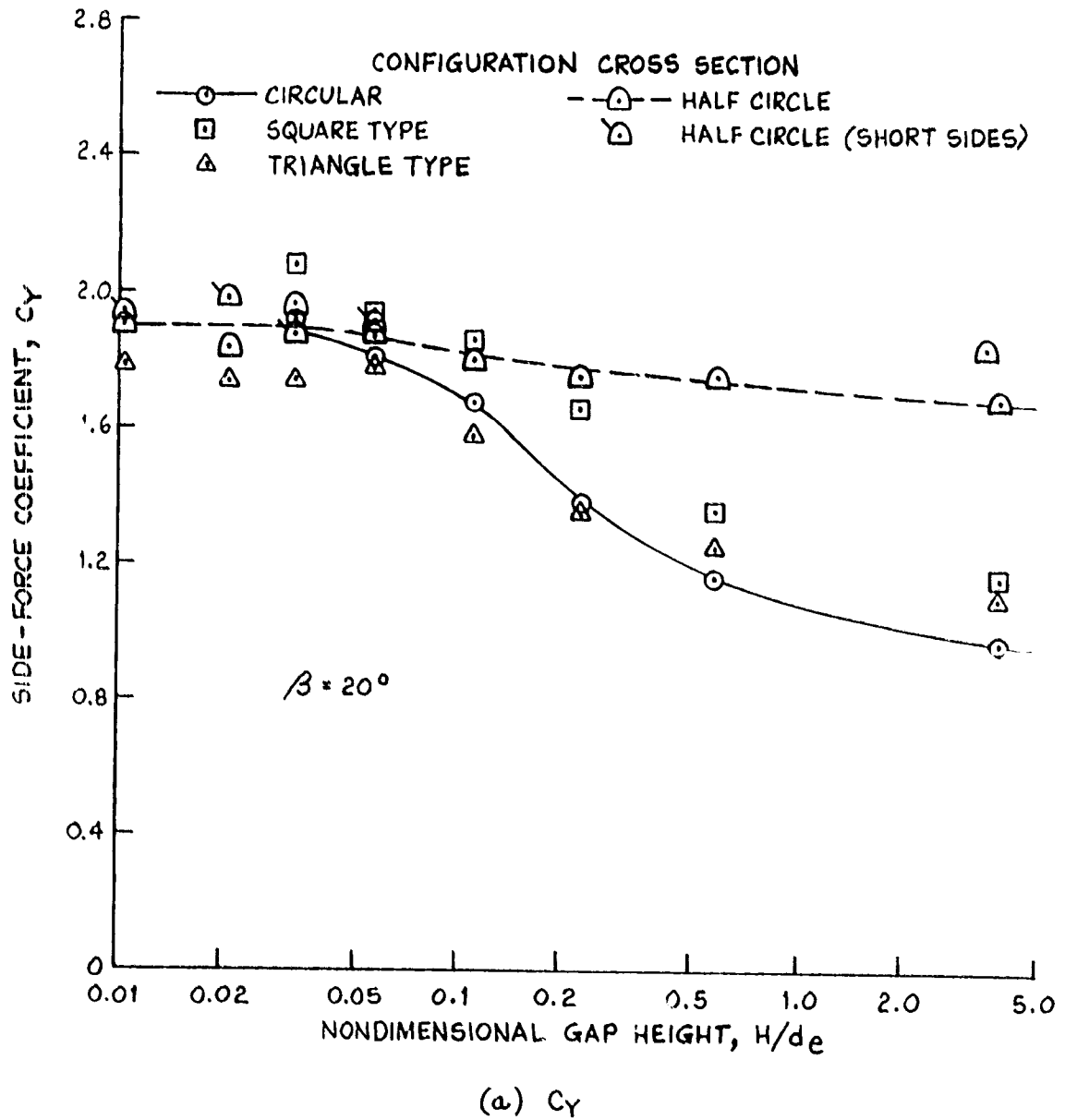
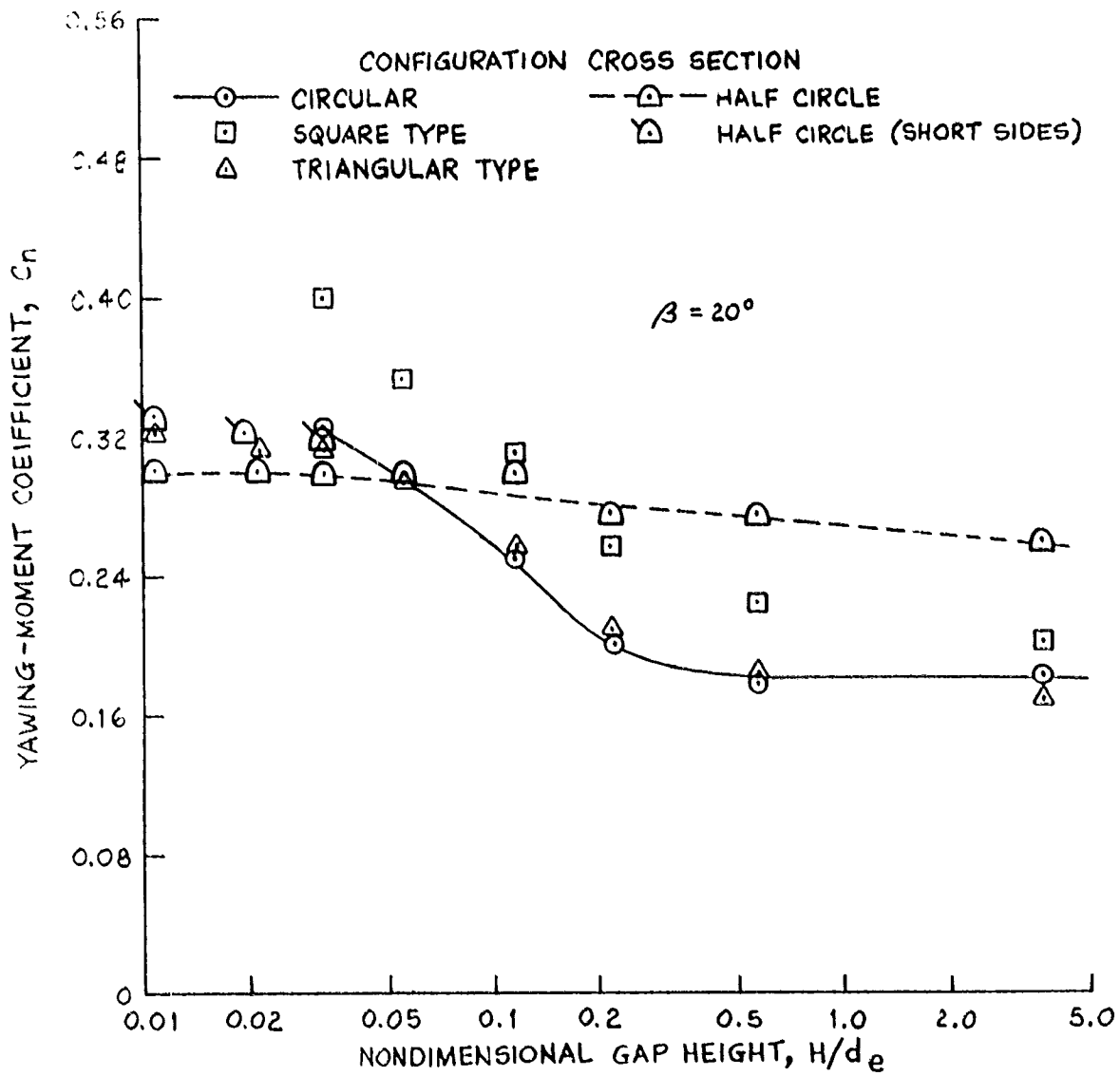
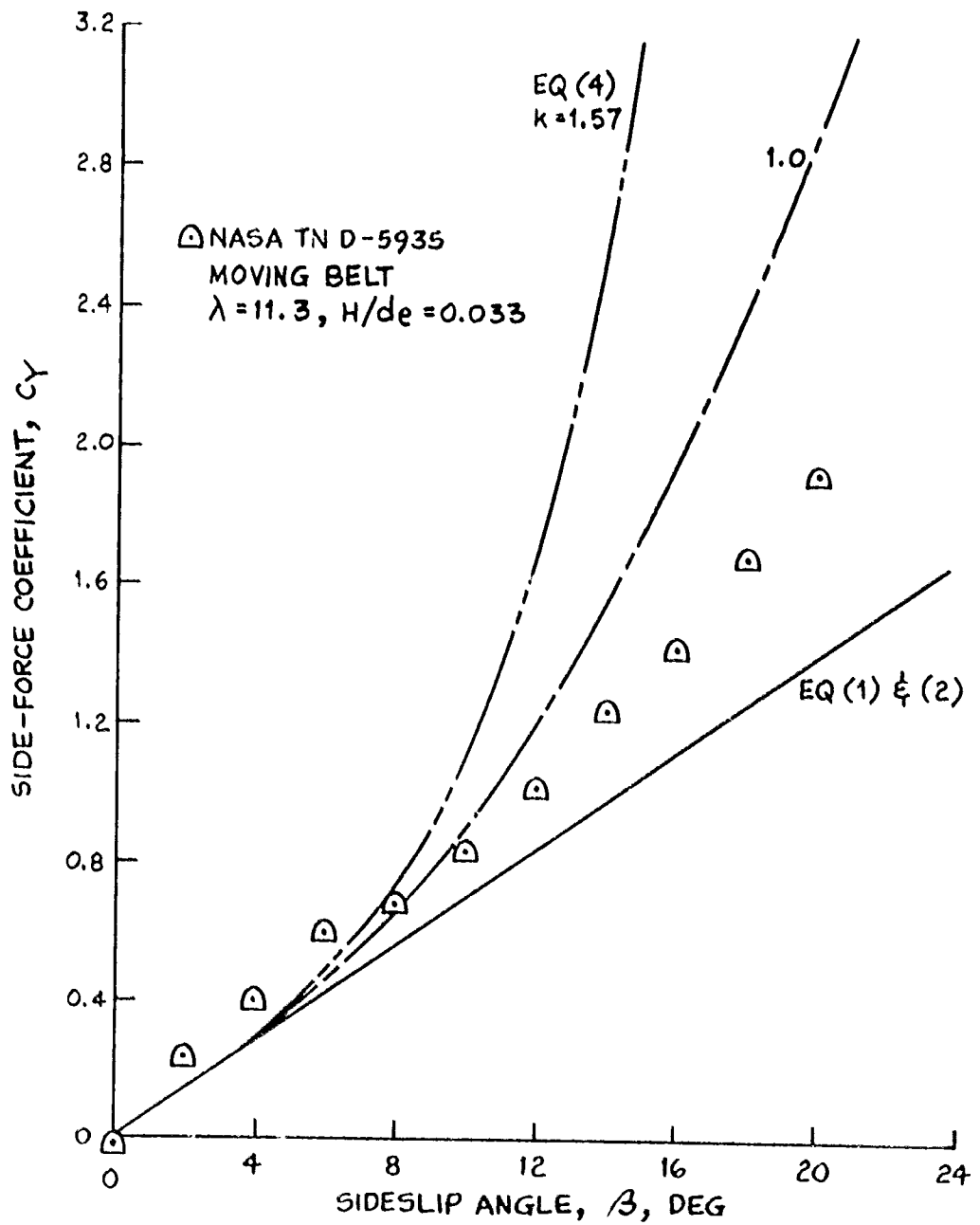


Figure 5 - Aerodynamic Coefficient Based on Area of Circle Having Diameter Equivalent to Vehicle Height Plotted as Function of Gap Height Above Ground for Six Configurations Tested by Grunwald, NASA TN D-5935.



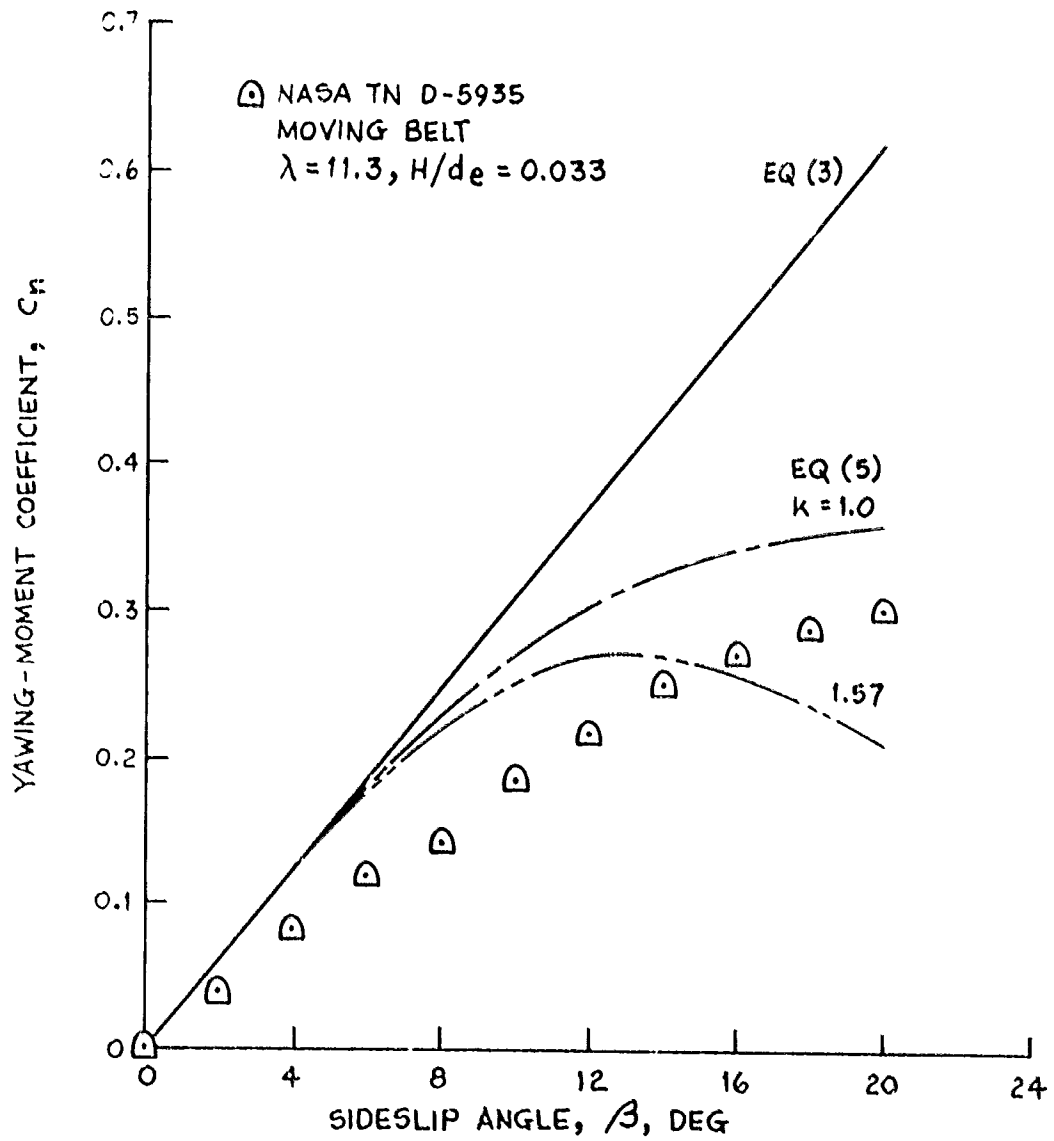
(b) C_n

Figure 5 - (Concluded)



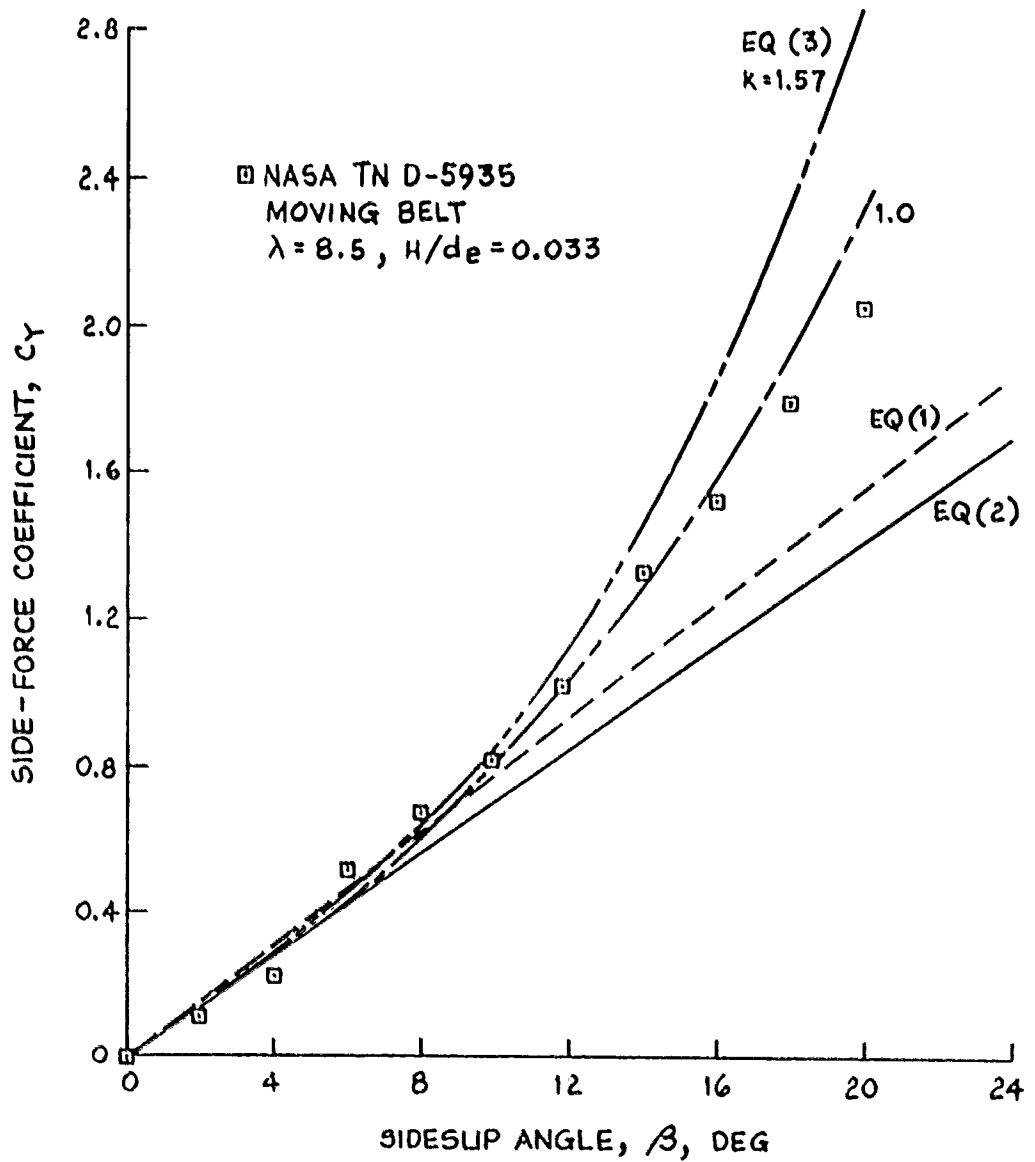
(a) C_Y

Figure 6 - Variation of Aerodynamic Coefficient With Sideslip Angle for Half Circle-Cross Section Configuration.



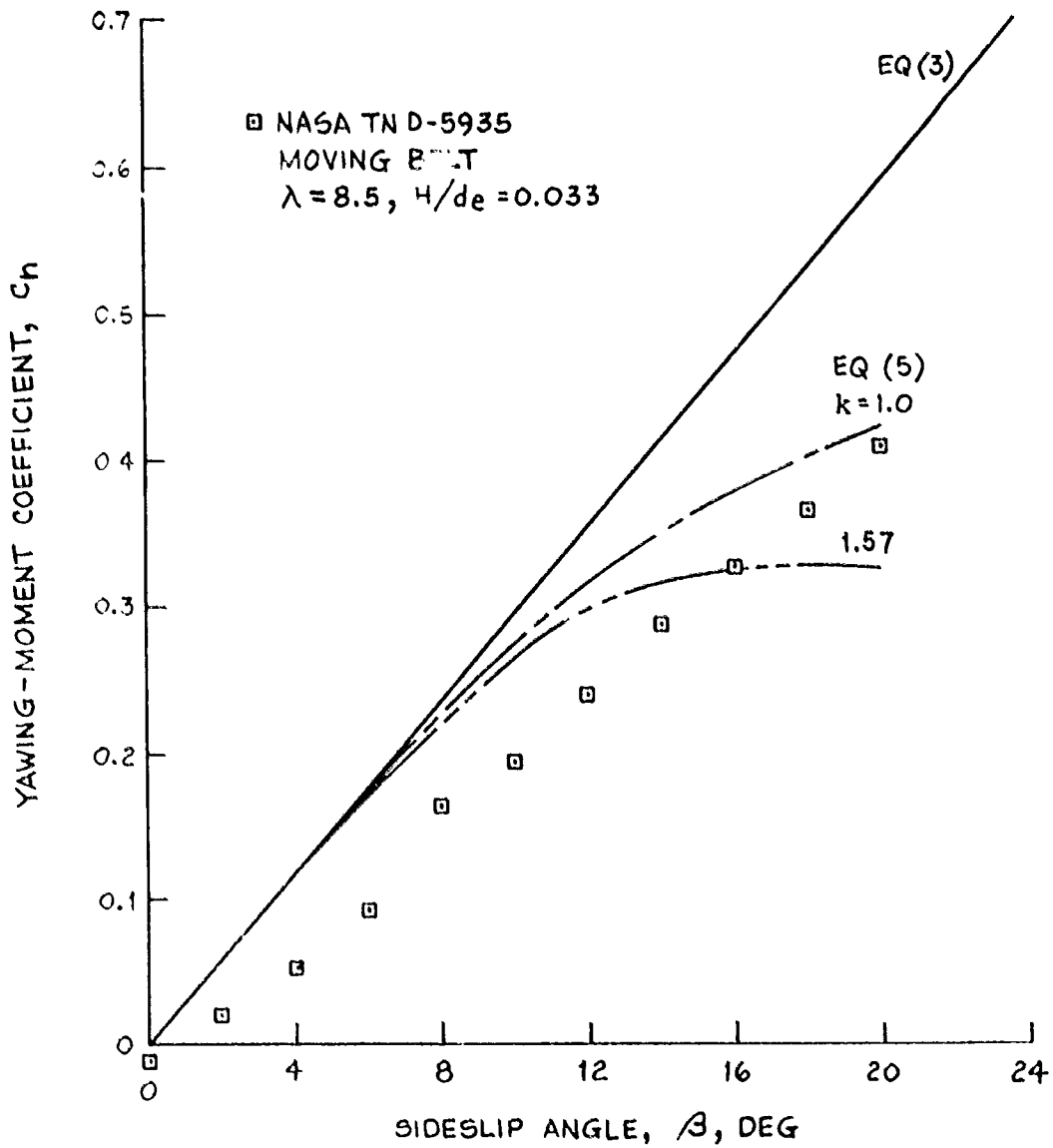
(b) C_n

Figure 6 - (Concluded)



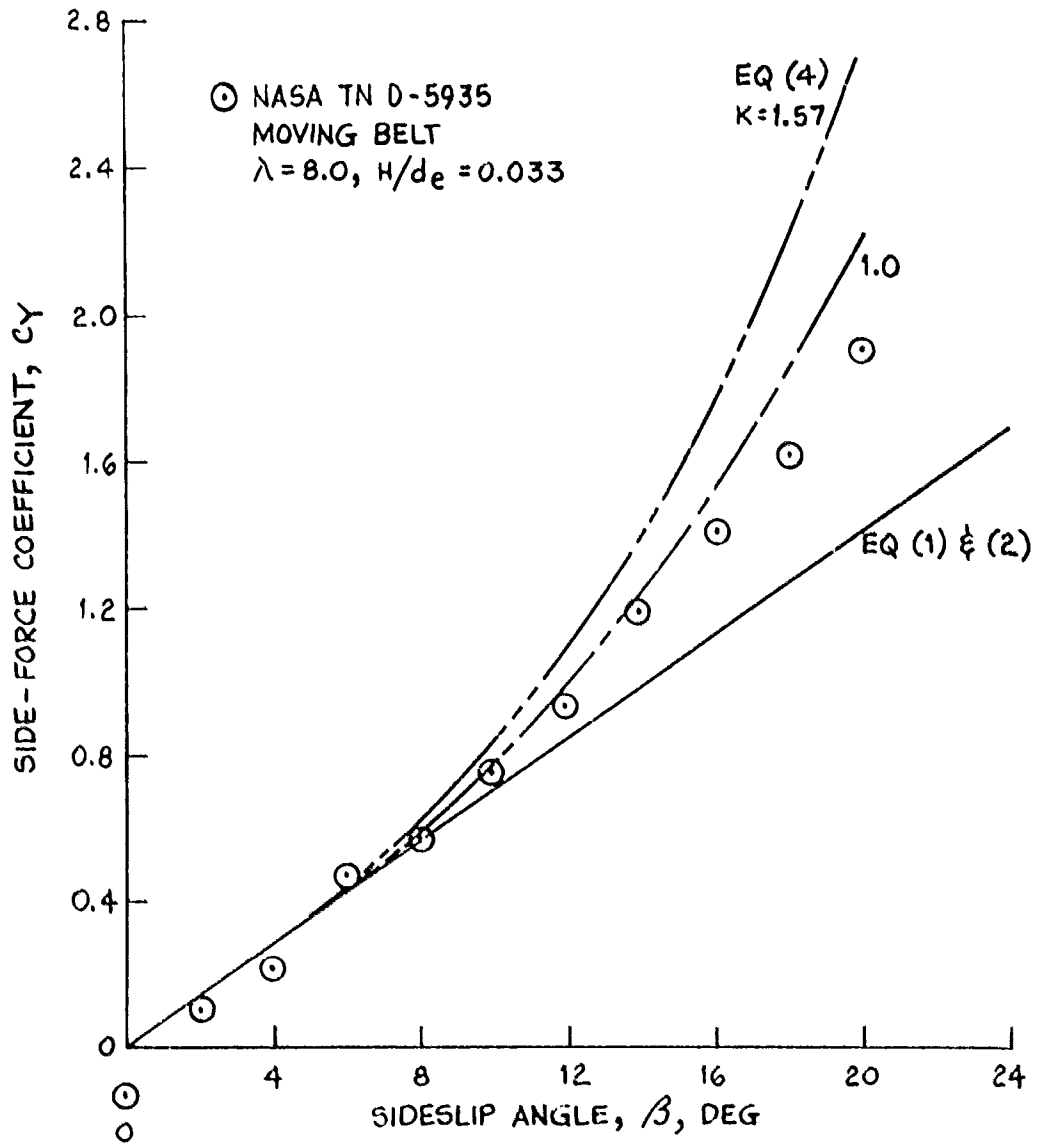
(a) C_Y

Figure 7 - Variation of Aerodynamic Coefficient With Sideslip Angle for Square Type-Cross Section Configuration.



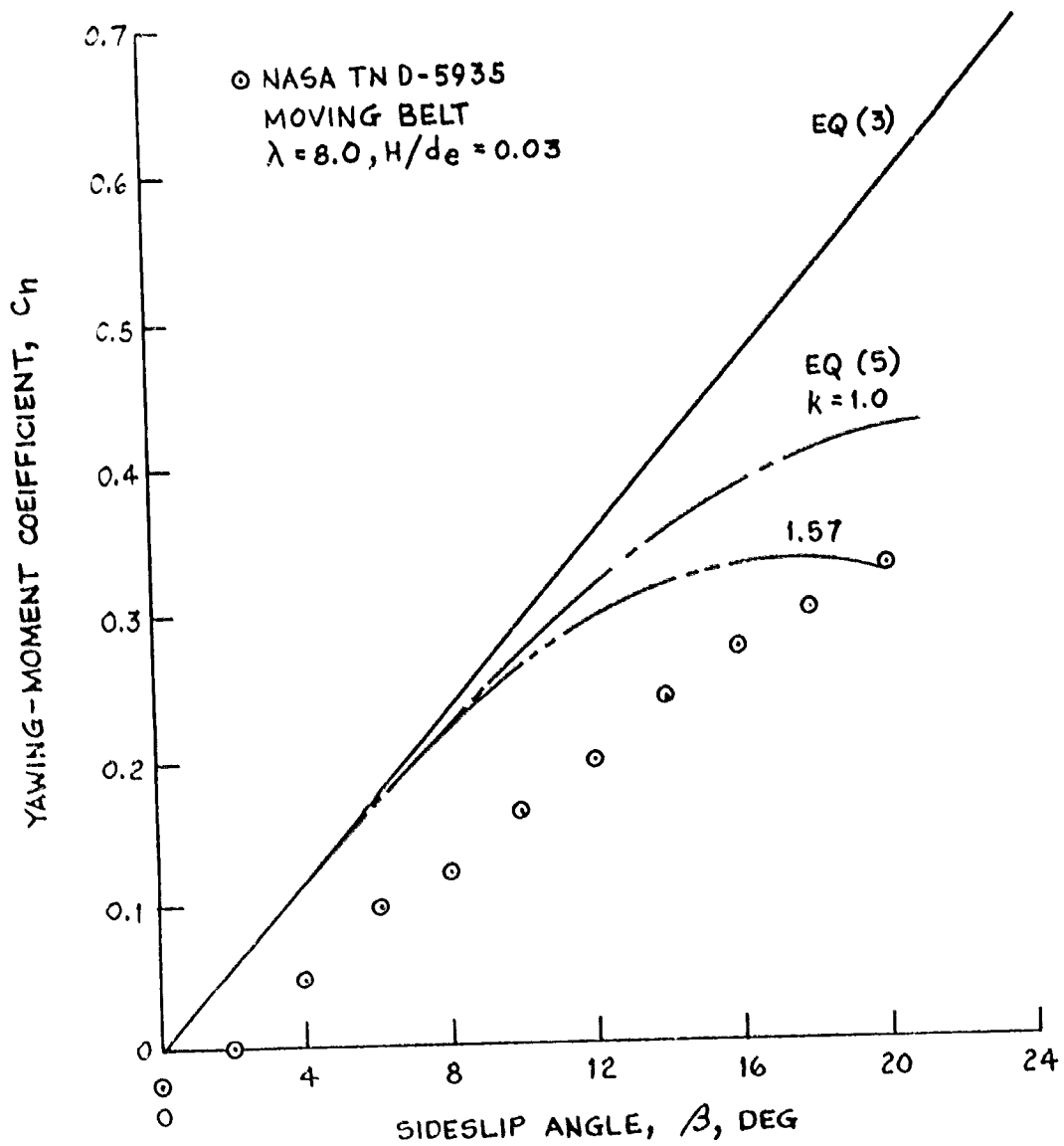
(b) C_n

Figure 7 - (Concluded)



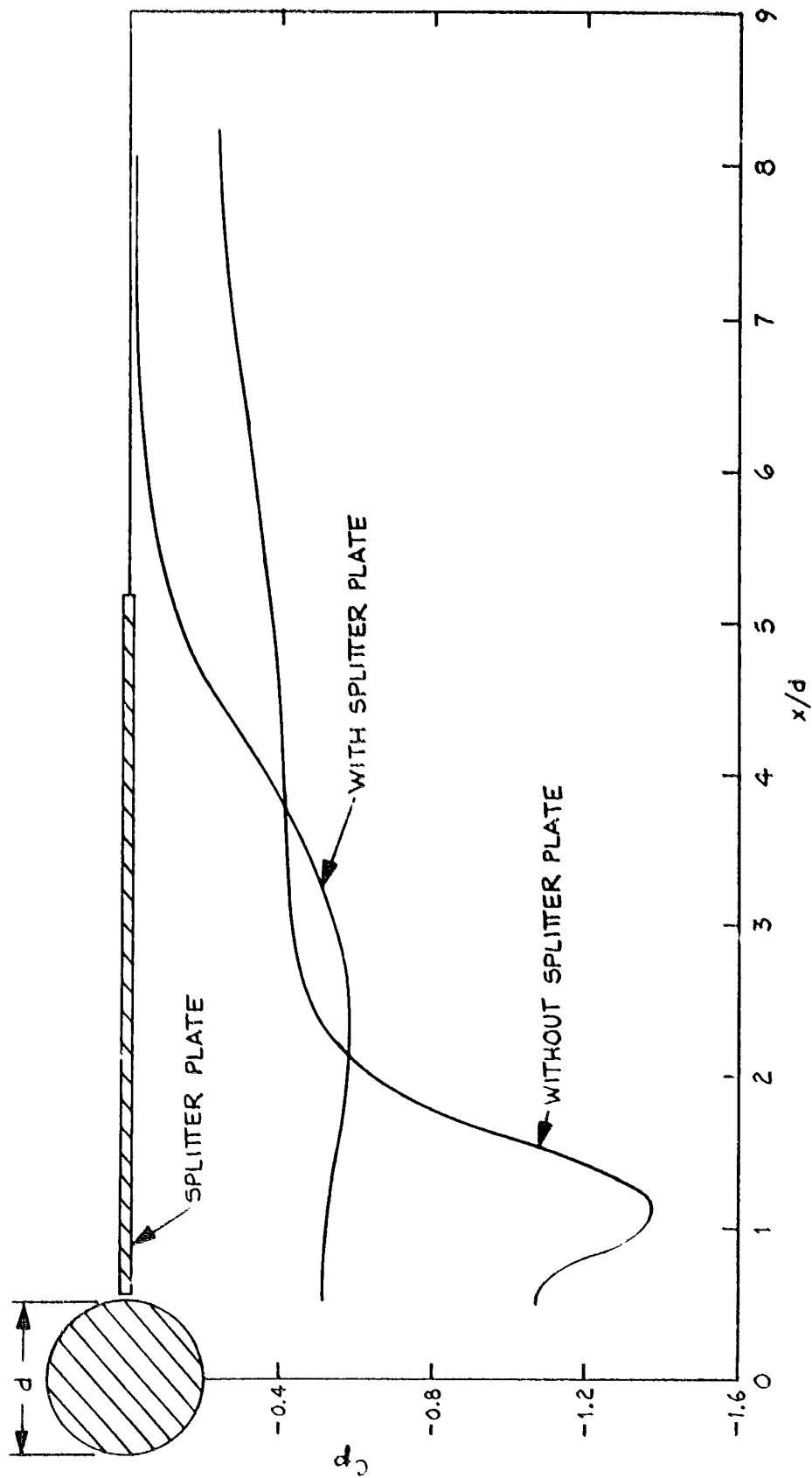
(a) C_Y

Figure 8 - Variation of Aerodynamic Coefficient With Sideslip Angle for Circular-Cross Section Configuration.



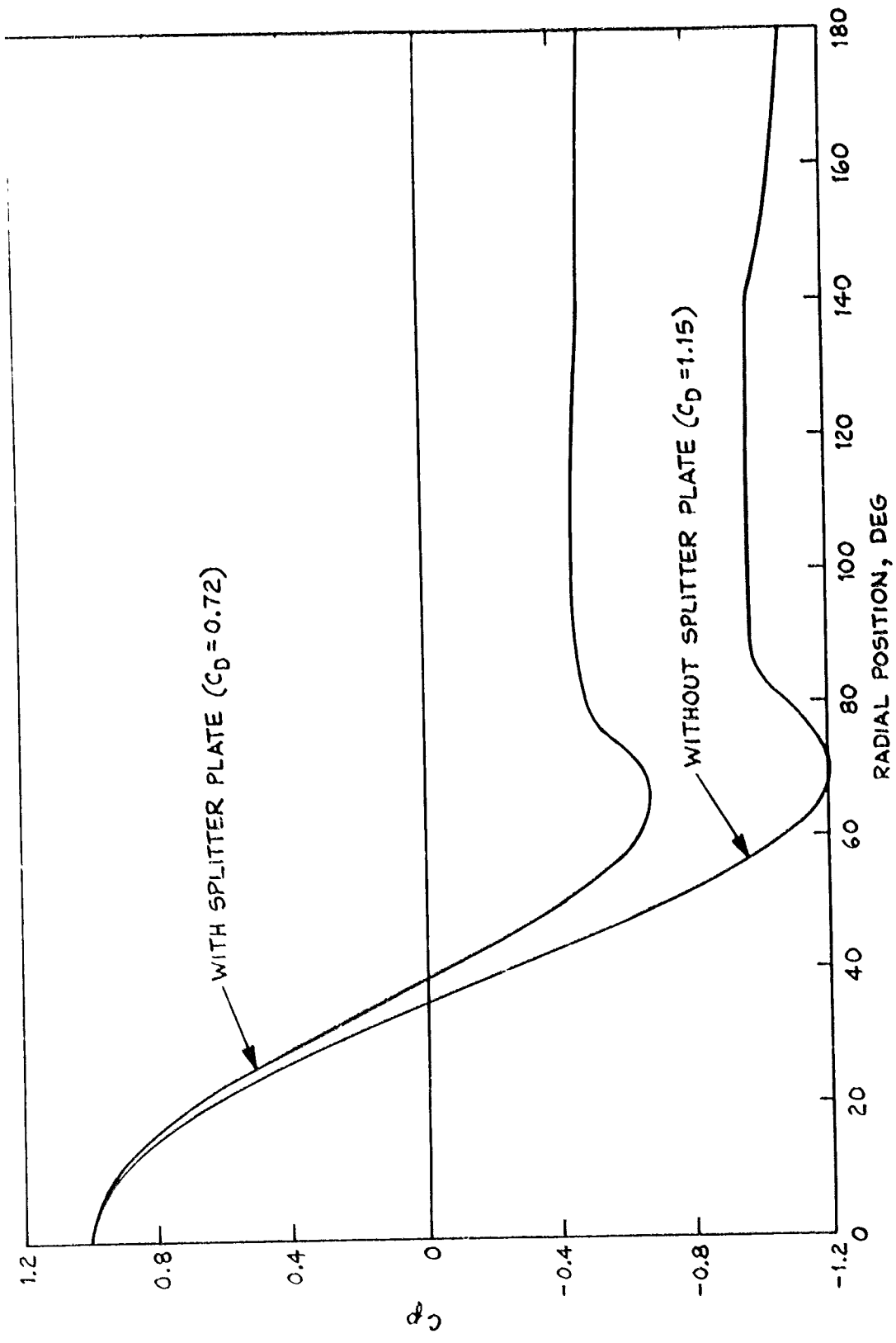
(b) C_n

Figure 8 - (Concluded)



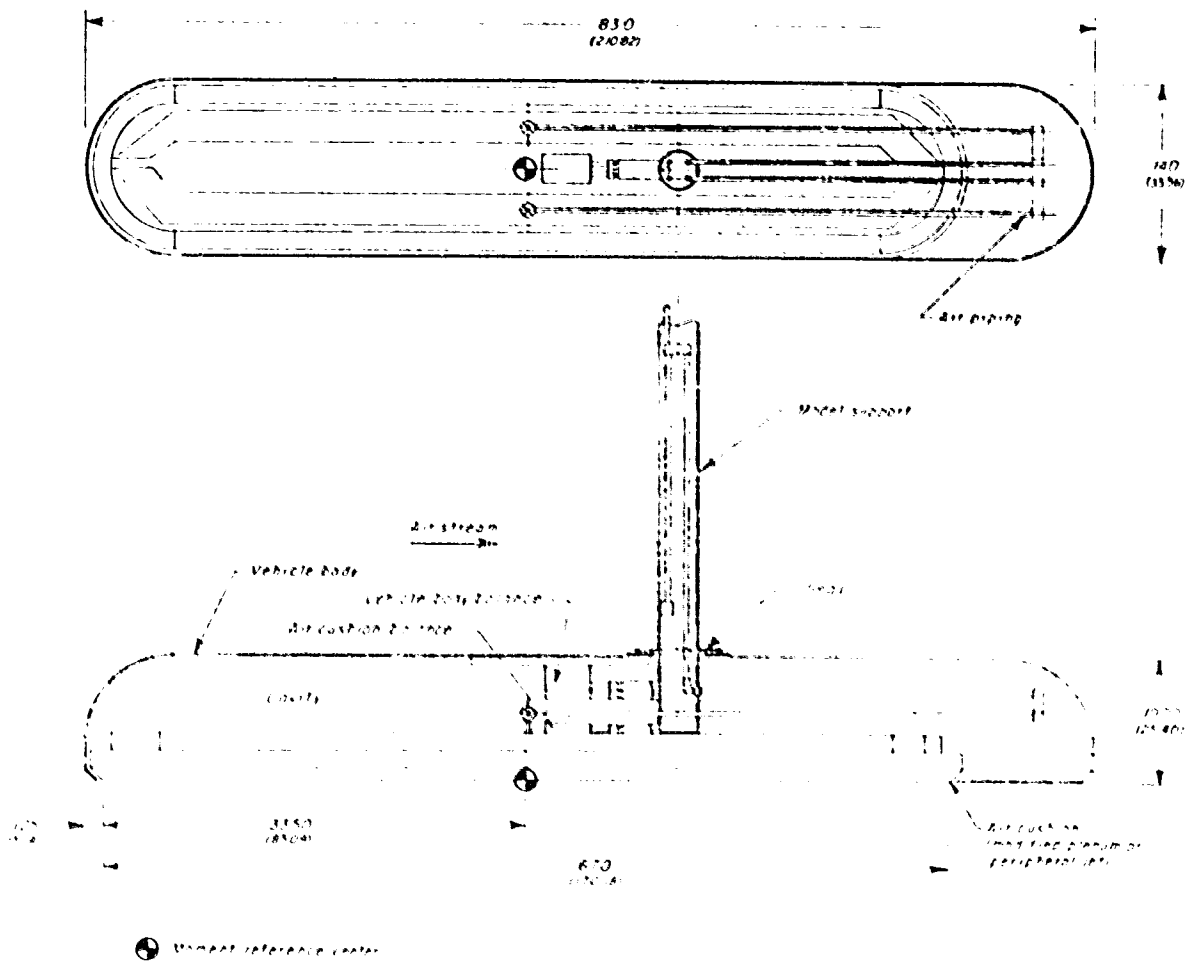
(a) PRESSURE ON WAKE CENTER LINE WITH & WITHOUT SPLITTER PLATE

Figure 9 - Effect of Splitter Plate in Wake of Circular Cylinder on Pressure. Roshko, NACA TN 3169.



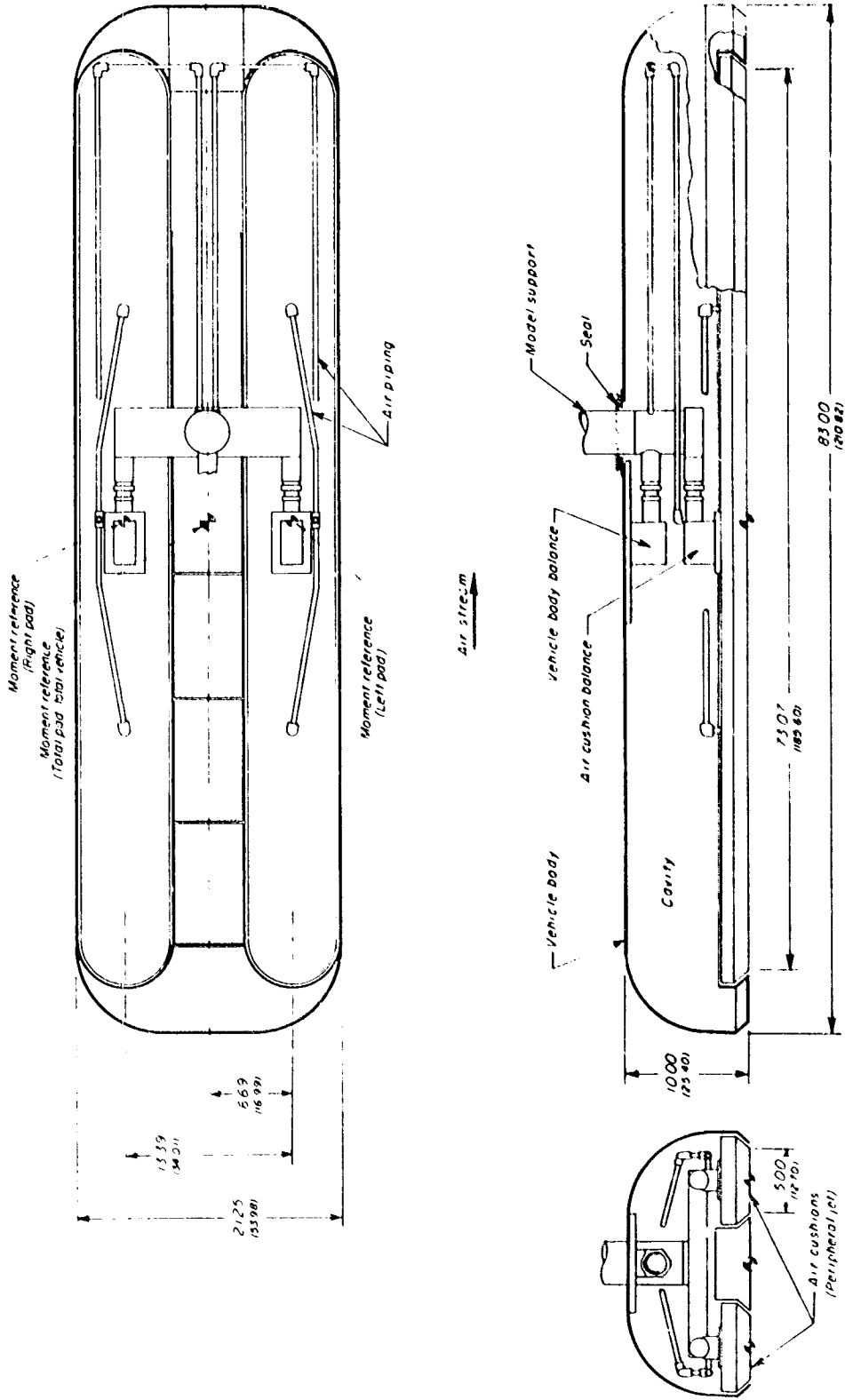
(b) PRESSURE ON CYLINDER

Figure 9 - (Concluded)



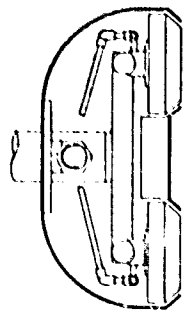
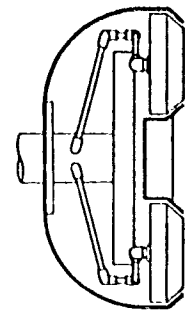
(a) Rectangular-type model.

Figure 10 - Sketches of three Models Employed by Grunwald and Johnson, NASA TN D-6011. All Dimensions are in Inches (Centimeters).



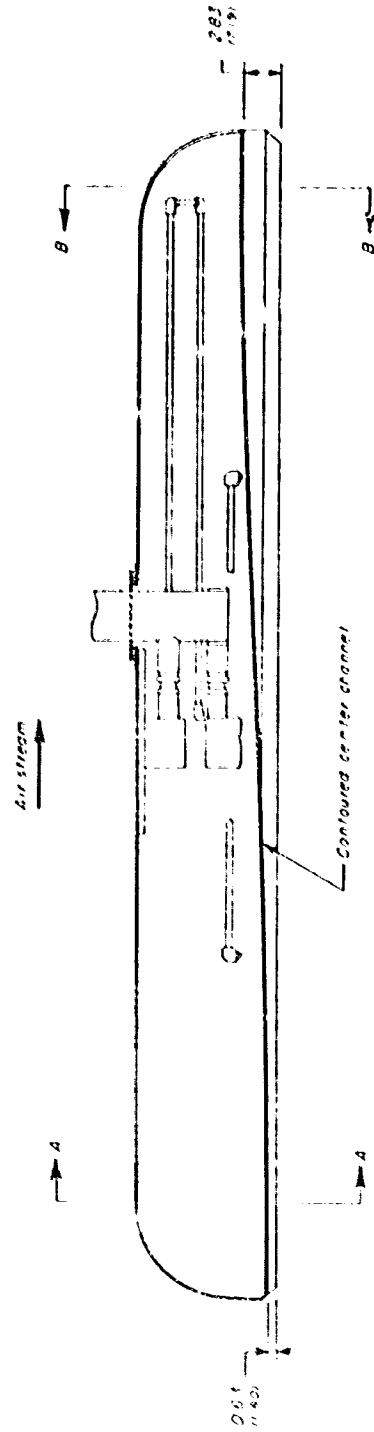
(b) Side-by-side model (flat-bottom configuration).

Figure 10 - (Continued)



View B

View A



(c) Side-by-side model (contoured-channel configuration).

Figure 10 - (Concluded)

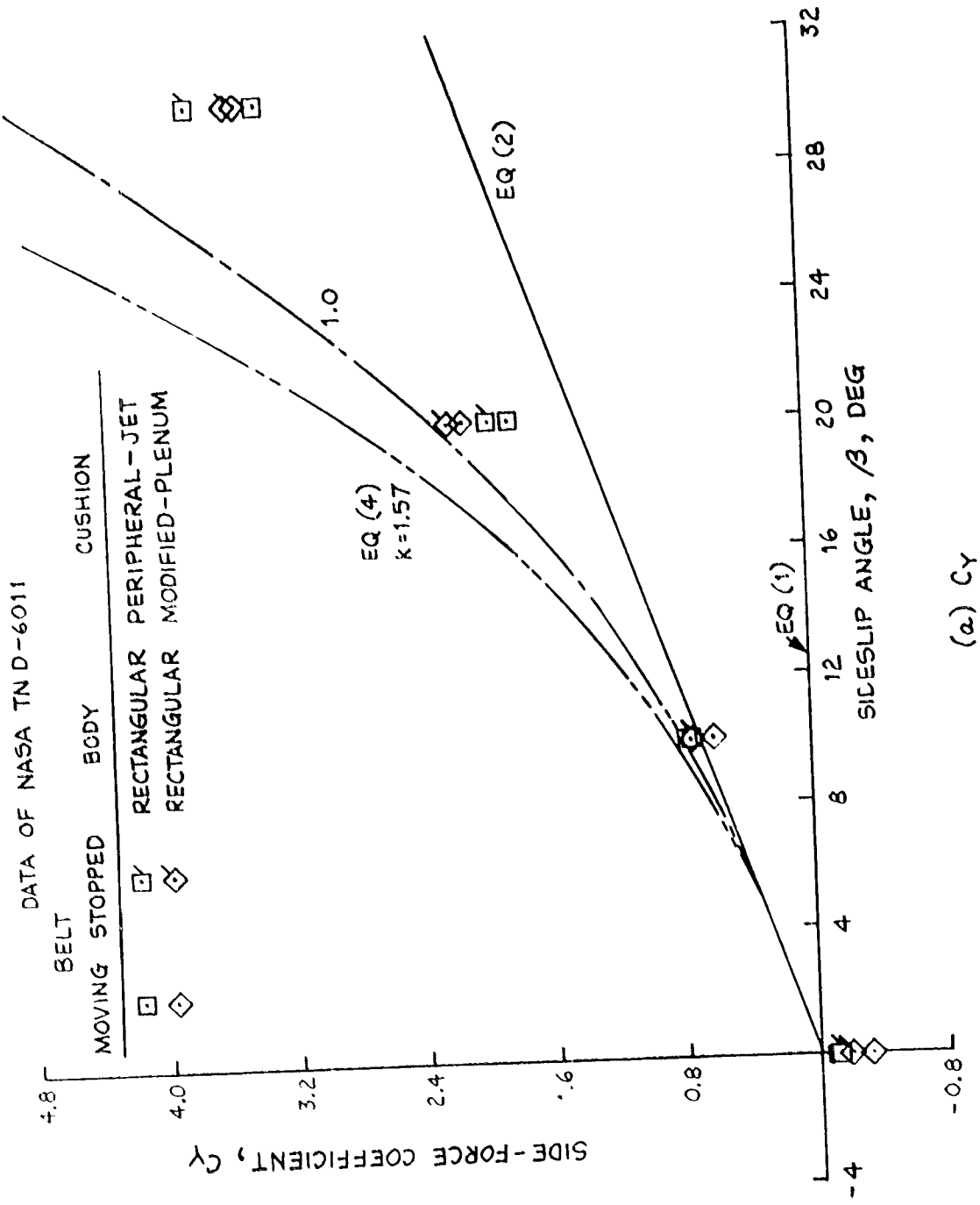


Figure 11 - Variation of Aerodynamic Coefficient With Sideslip Angle for Rectangular Air-Cushion Models.

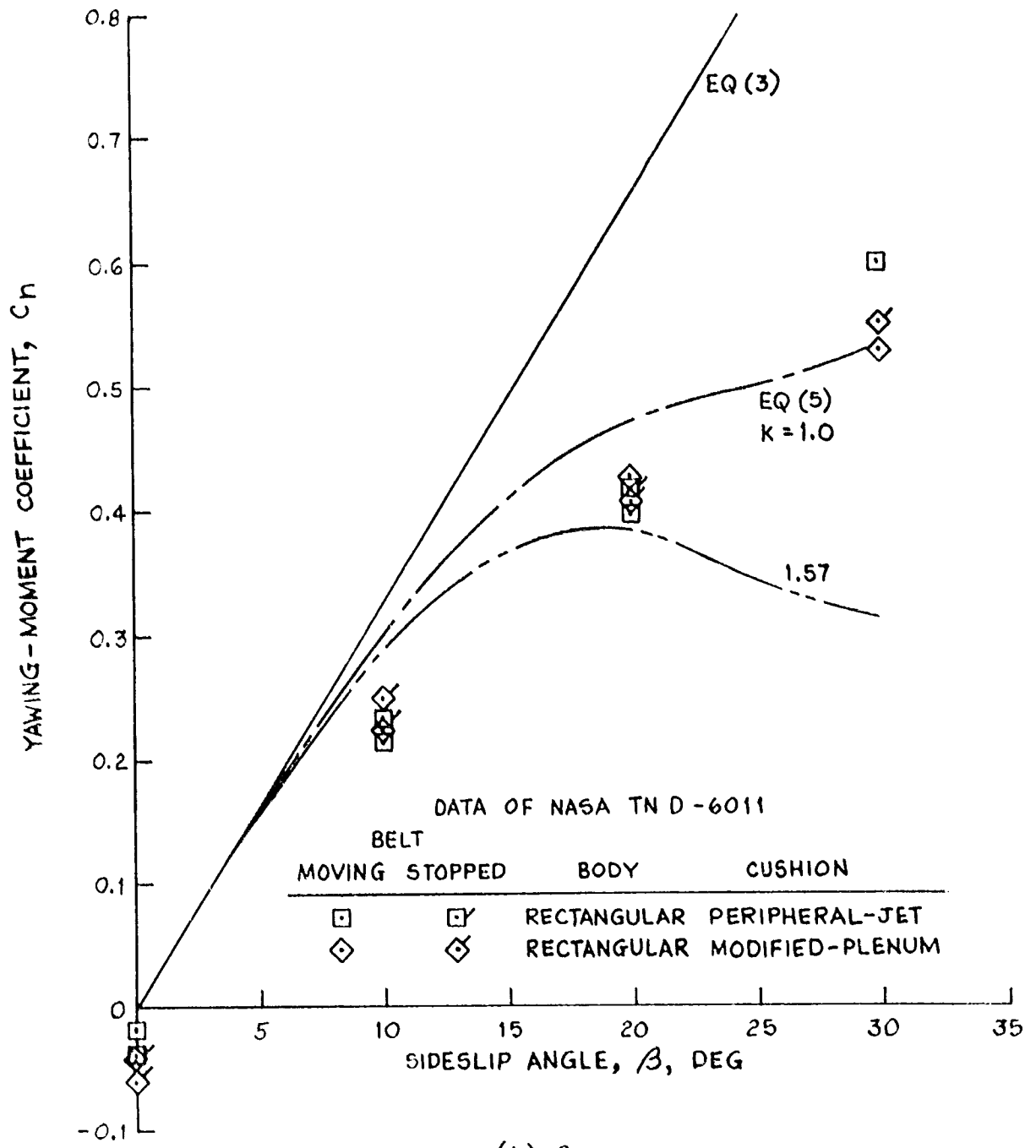
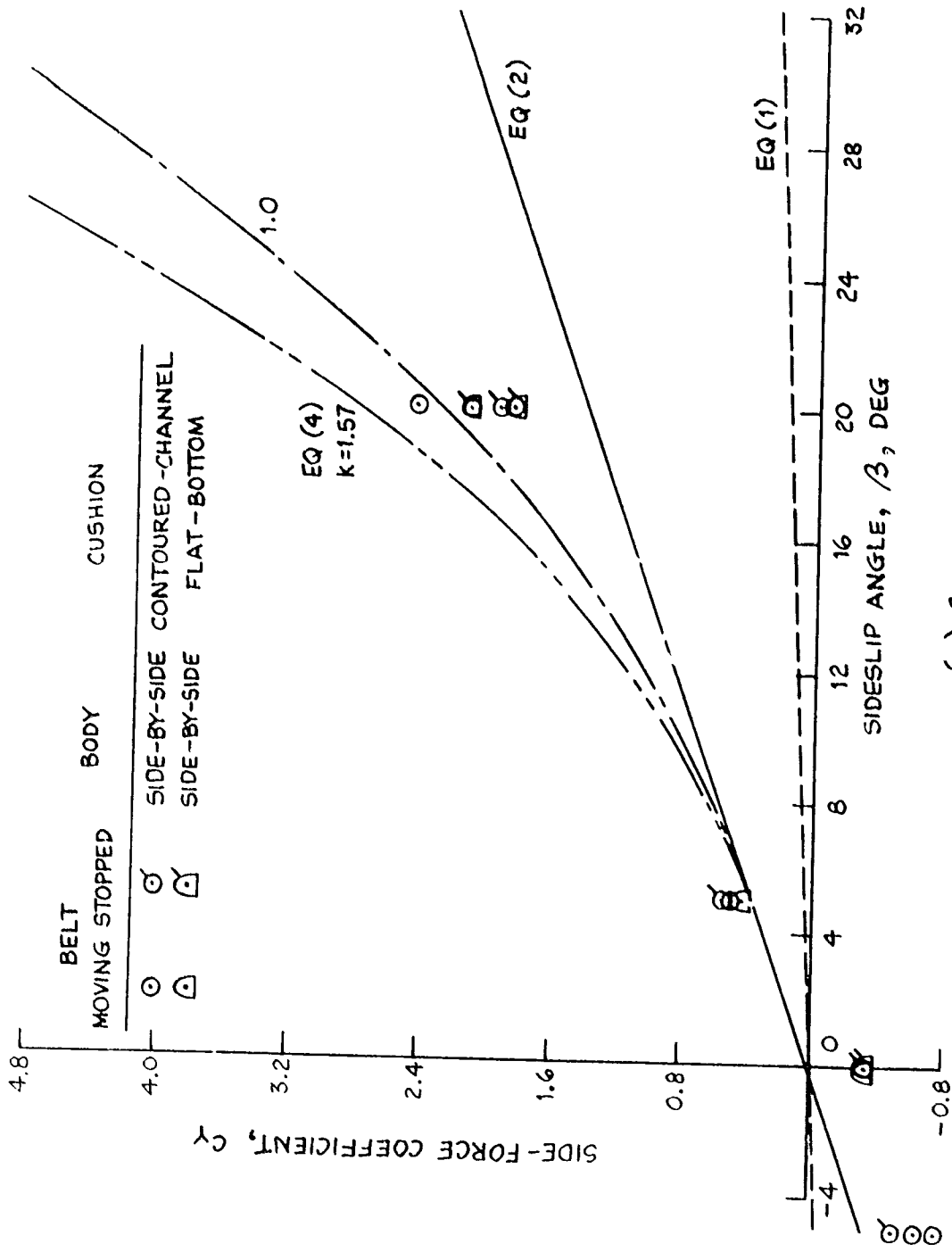


Figure 11 - (Concluded)



(a) C_Y

Figure 12 - Variation of Aerodynamic Coefficients with Sideslip Angle for Side-by-Side Air Cushion Models.

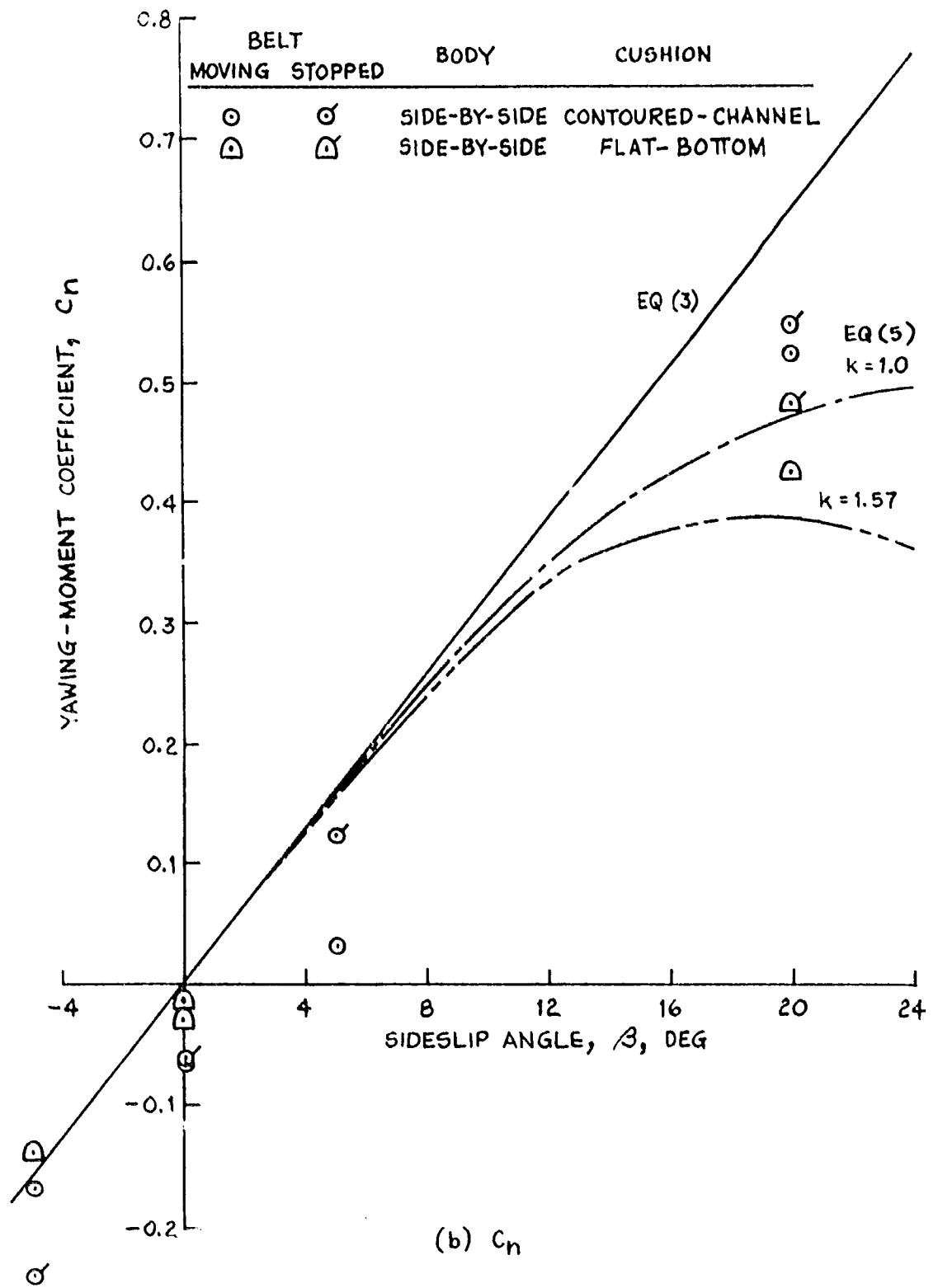


Figure 12 - (Concluded)

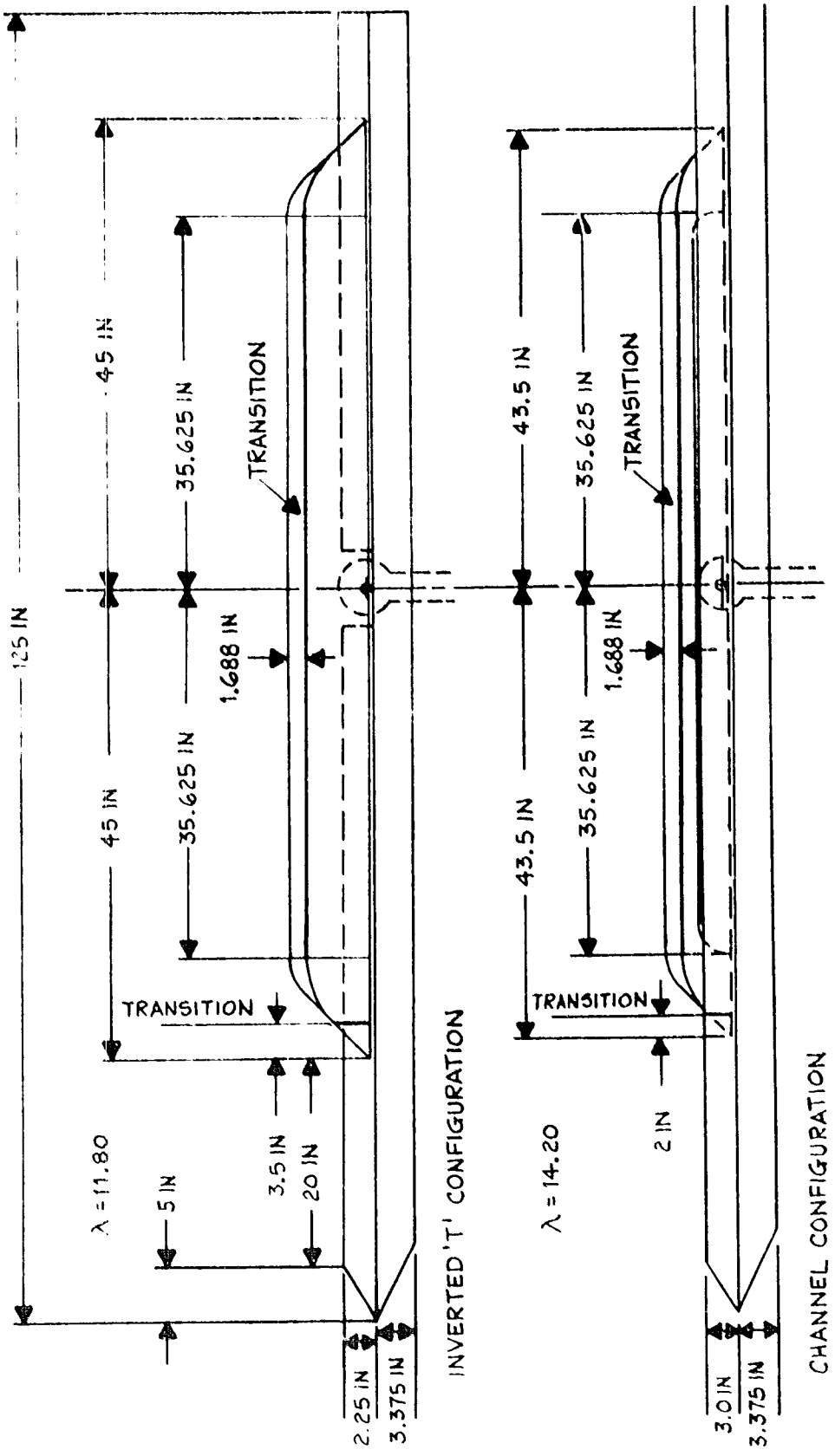
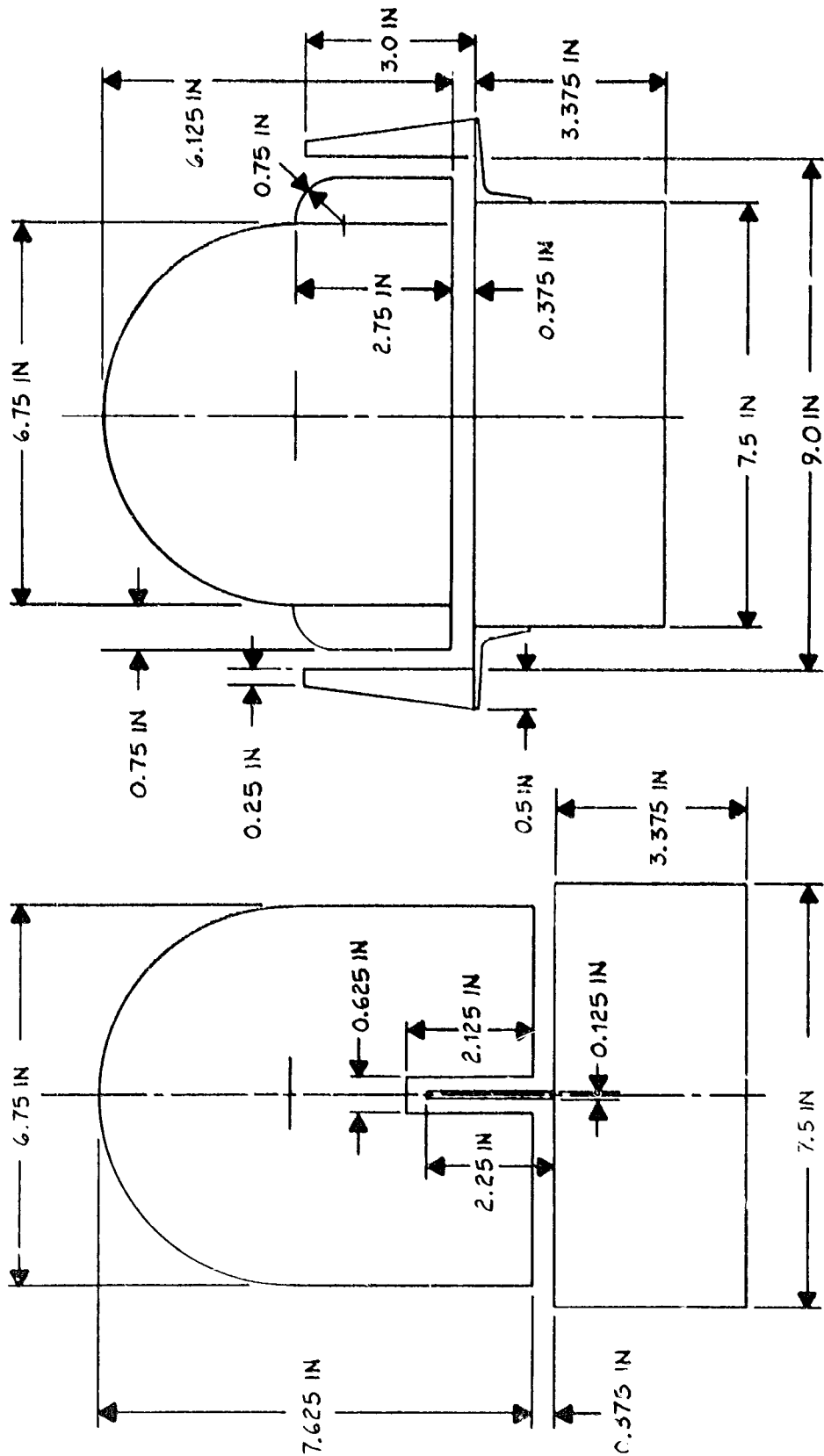


Figure 13 - Dimensions of Track and Vehicle Models, THL, FRA-RT-71-68.



(a) INVERTED 'T' CONFIGURATION
 (b) CHANNEL CONFIGURATION

Figure 14 - Dimensions of Track and Vehicle Models, THL, FRA-RT-71-68.

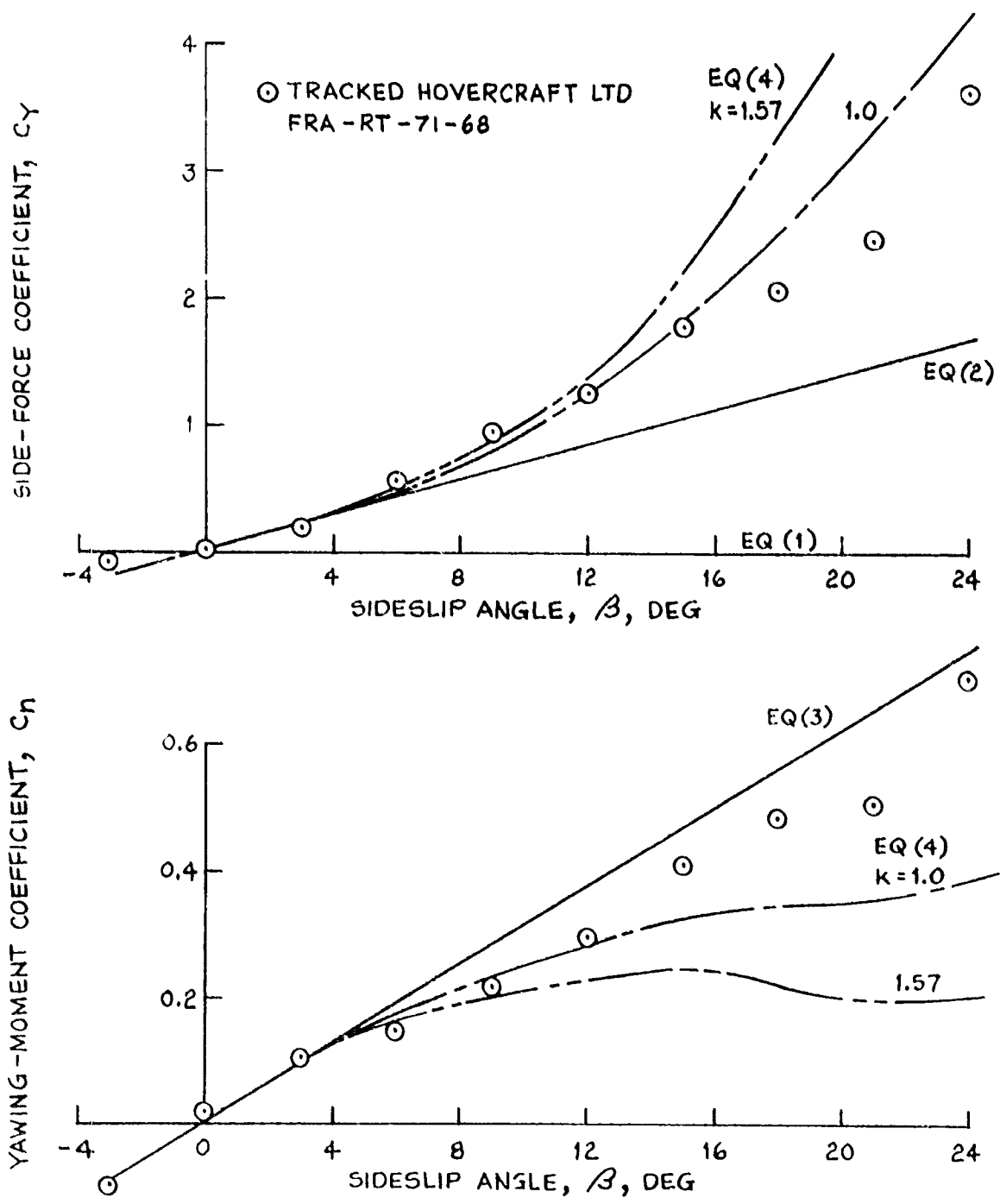


Figure 15 - Effect of Yaw Angle on Sideforce and Yawing Moment Coefficients, Inverted T Configuration. $\lambda = 11.8, \gamma = 0.$

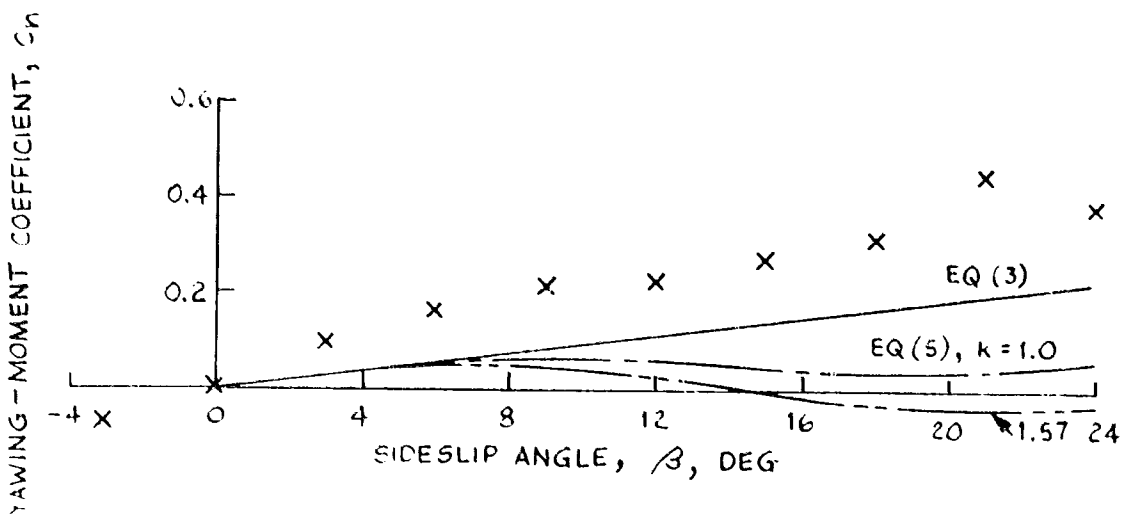
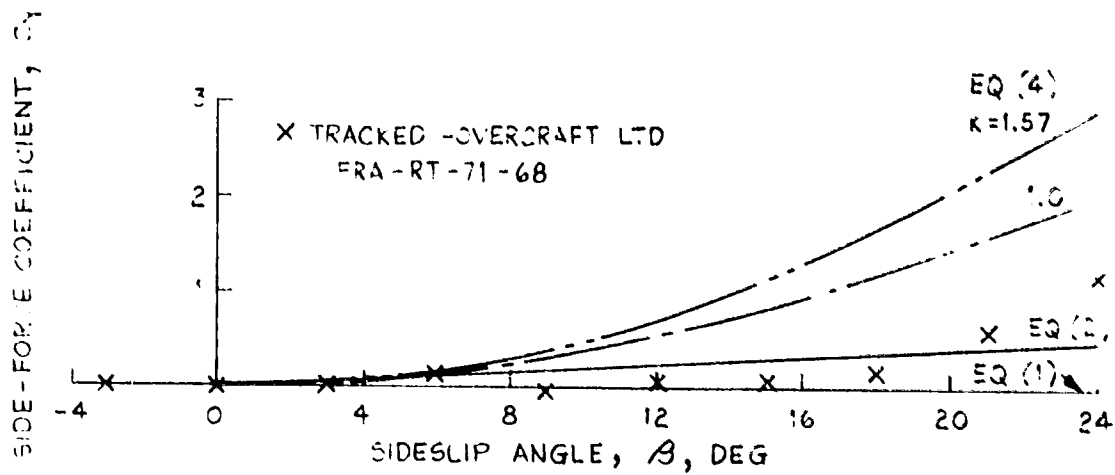
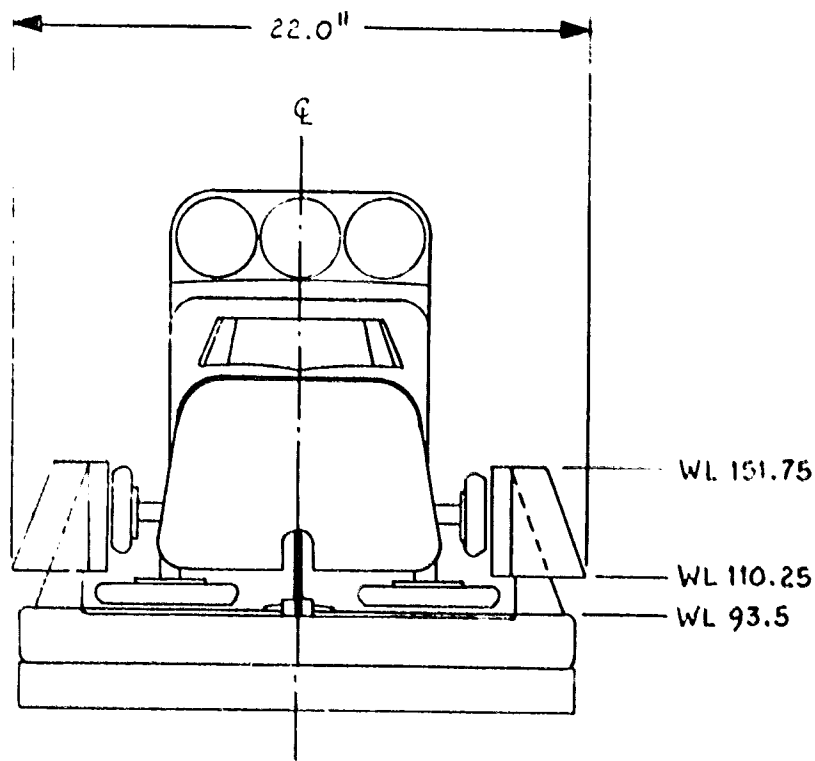


Figure 16 - Effect of Yaw Angle on Sideforce and Yawing Moment Coefficients, Channel Configuration. $\lambda = 14.2$, $\gamma = 0.43$.



(a) FRONT VIEW

Figure 17 - Sketch of 1/10-scale Model Used in Gruman Tests,
PMT-B4-R71-06.

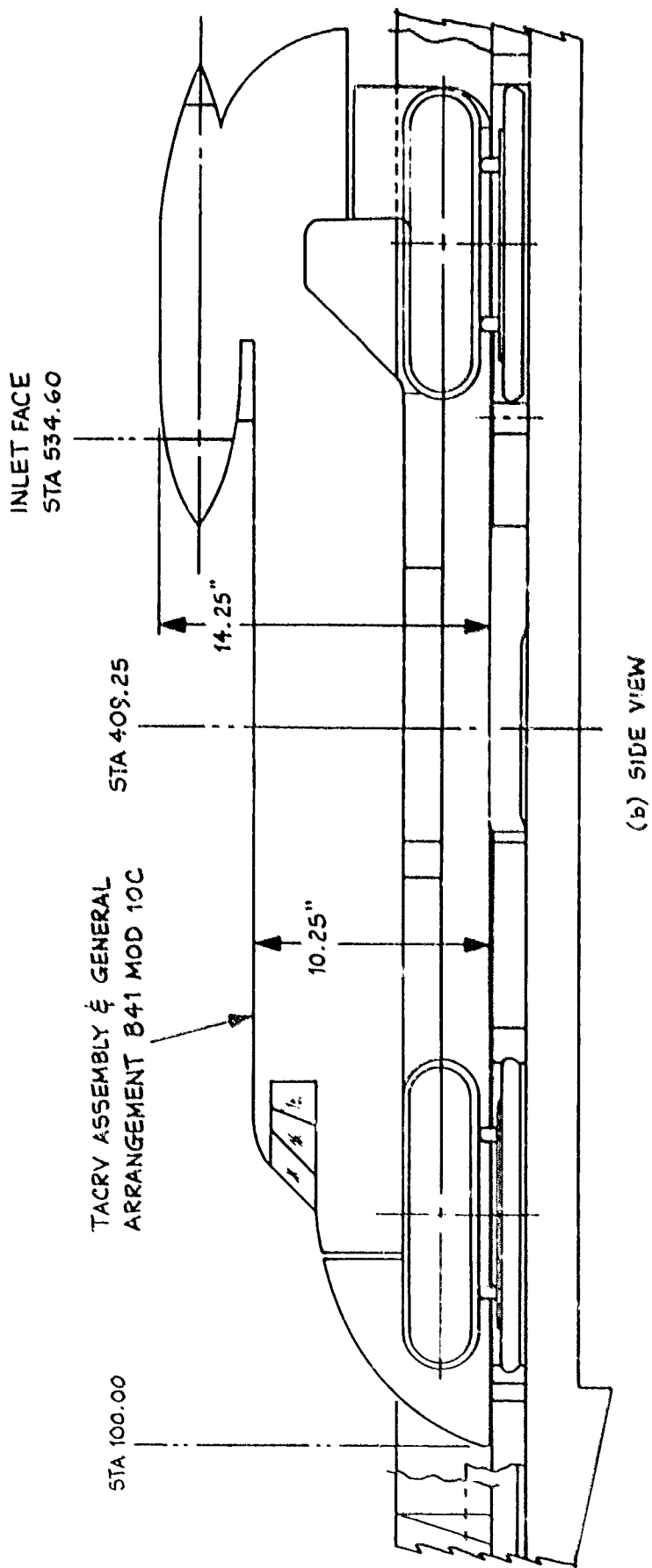


Figure 17 - (Concluded)

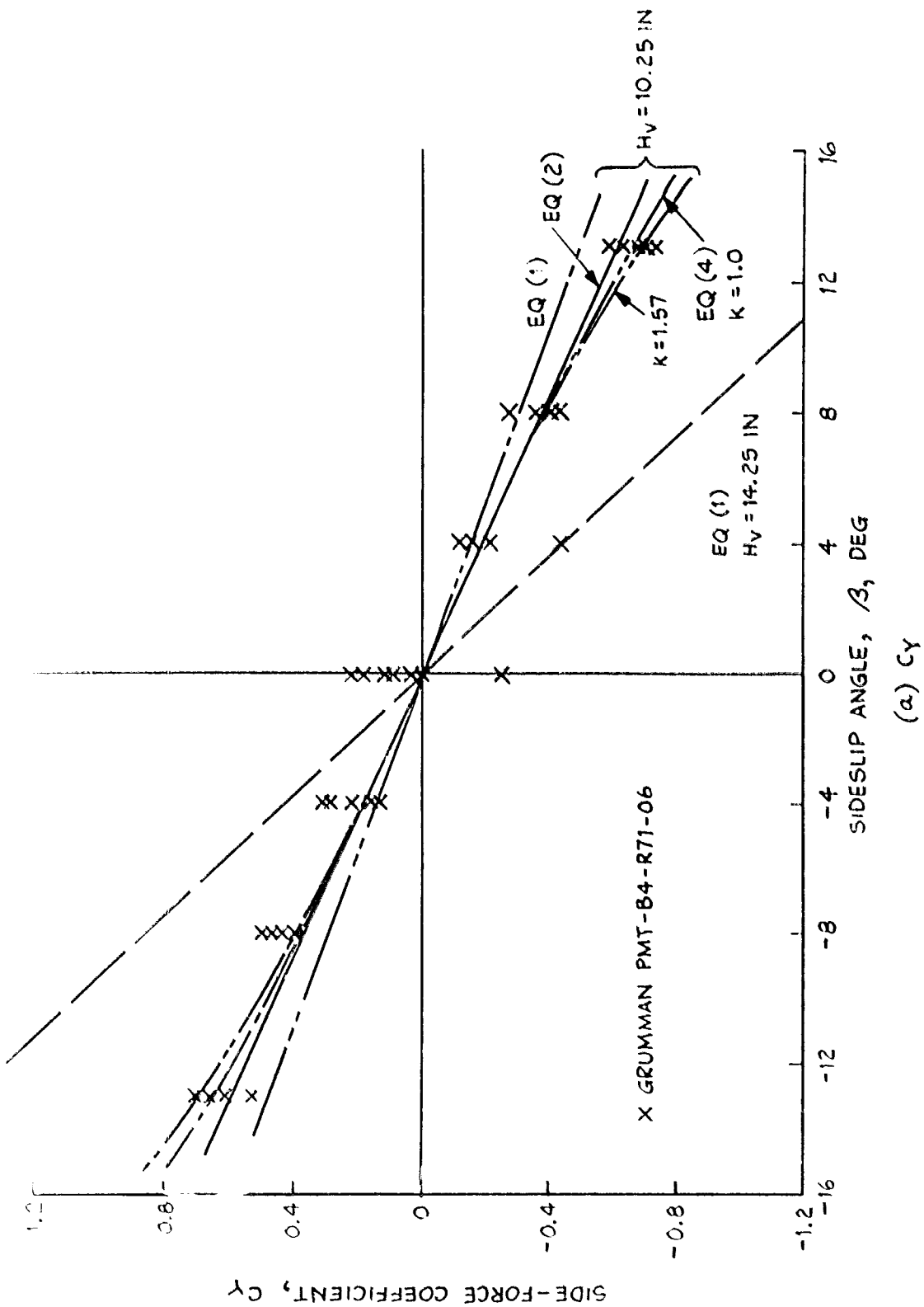
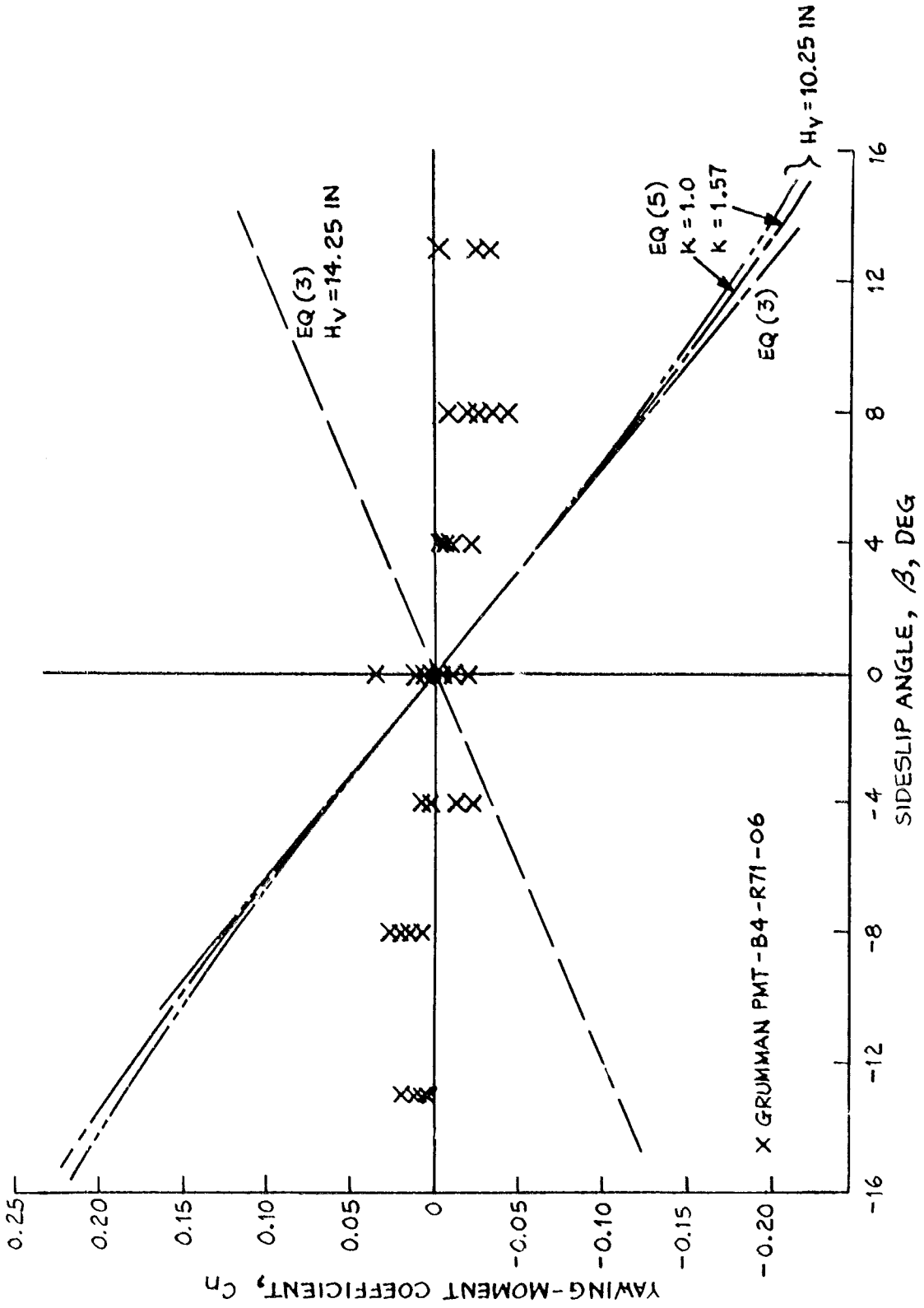


Figure 18 - Variation of Aerodynamic Coefficients With Sideslip for TACRV Model. C_y and C_n are Defined Using $H_V = 10.25$ inches for Test Data.



(b) C_n

Figure 18 - (Concluded)

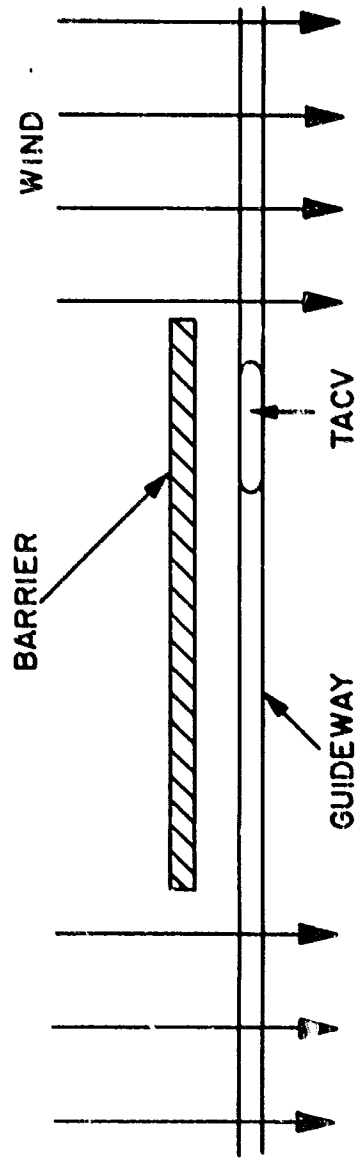


Figure 19 - Sketch of a Test Arrangement for Measuring Airloads due to Side Wind and Gust